

UNIVERSITY OF CALIFORNIA,
IRVINE

Modelling the mechanics of the plasma membrane and nuclear envelope: dynamics and
disease

ADVANCEMENT TO PHD CANDIDACY
in Mathematical and Computational Biology

by

Kathryn Manakou

Advancement Committee:
Dr. Jun Allard, Chair
Dr. German Enciso
Dr. Anya Grosberg
Dr. John Lowengrub
Dr. Michael Zaragoza

2017

© 2017 Kathryn Manakou

TABLE OF CONTENTS

1. Abstract

It is becomingly increasingly obvious that for particular cellular functions, biomechanics plays a central role. We use a combination of biomechanics and chemical reaction modelling frameworks to study biological processes at the cellular level. In particular, we are studying the mechanical properties of the filamentous networks on the inner face of biological membranes. In the case of cell membranes, an underlying actin cortex acts to maintain cell shape and rigidity. Disruptions in the cortex lead to transient membrane protrusions known as blebs, which are implicated in a variety of cellular functions. Here, we developed a model which recapitulates the bleb life cycle and provides conditions under which blebbing occurs. Furthermore, our model can give rise to travelling blebs, a mysterious behaviour observed in some cell lines, and predicts travelling velocity, which had not been established by other models. The fast-slow dynamics of the model leads to interesting mathematical behaviours, such as a canard explosion associated with a supercritical hopf-bifurcation, which we plan to characterize in greater detail in the future. We have also derived a previously unknown necessary condition for travelling wave solutions to exist in such a system, and demonstrate sufficiency numerically. Nuclear blebs, as distinct from cellular blebs, are nuclear shape deformations often resulting from mutations in the gene encoding for lamin A/C, a major component of the filamentous network underlying the nuclear envelope. The specific defect in the mutated lamin proteins is unknown, as is the mechanism by which nuclear blebs form. We are developing mathematical models of the nuclear lamina in order to probe various portential defects in lamin proteins and correlate the resulting simulated nuclear shapes with patient and control data obtained from our collaborators in the Department of Biomedical Engineering and the School of Medicine.

2. Introduction

It is known that both chemical dynamics and mechanics play important roles in biological systems. One approach to studying the interplay between the two is through mathematical modelling. The application of mathematical models to the field of biology has a long history but with more recent technological advances in things like computational power, the type of models we can build and simulate are becoming ever more complex and holistic. Similarly, with renewed focus on bridging the gaps between physics, mathematics and biology more elaborate biophysical model have been developed and simulated. Here, we developed biophysical models to study the membrane mechanics of eukaryotic cells and the nuclear lamina in animal cells.

The eukaryotic cell membrane acts as the main barrier between the cell and the surrounding environment. Inside the cell, the membrane is supported by a dense networks of actin filaments called the cortex which is attached to the cell membrane via adhesion molecules. The cortex maintains the cell shape and contracts inward generating internal pressure in the cell. Local disruptions to the cortex result in dynamic, transient protrusions of the cell membrane termed blebs. Blebs are implicated in many cellular activities including apoptosis, mitosis and motility, yet little is known about the mechanism underlying bleb formation. One particular aspect which has received little attention is the travelling behaviour of some blebs around the cell periphery, which may have implications in bleb based motility. We use mathematical modelling to elucidate the mechanisms underlying this behaviour.

The equations arising from this study are interesting in their own right, as little research has been done for this class of integro-PDEs. More typical systems of equations arising in biological contexts, such as reaction-diffusion equations, have been studied extensively and many of their properties are well established. One such property is the existence of travelling wave solutions, which is known to be important to many biological processes. In the case of reaction-diffusion systems, the condition which allows for travelling wave solutions is known, in our case of a non-diffusion like system, it is not. We believe the class of equations which our system falls into can and will be used to describe other biological systems in the future and so we seek an analog to this which will be applicable to a particular class of integro-PDEs.

A superficially similar problem to that of cellular blebs is seen in the nuclei of animal cells. Nuclei are bounded by a double membrane, and this double membrane is supported by a dense networks of lamin filaments termed the nuclear lamina. In cases where the gene responsible for producing lamin A/C, the main constituent of the nuclear lamina, is mutated, a variety of disease states may ensue, including extremely severe diseases such as progeria and heart disease. The nuclei in these mutated cells often have irregular shapes, with one or more protrusions termed nuclear blebs. In this case, the blebs are not due to a disruption

in the linkage between the nuclear membrane and the lamina (as blebs contain lamina), but rather might due to a defect in the lamina itself. The mechanism by which nuclear blebs form is unclear. We use mathematical modelling to probe potential defects in the lamin A/C protein, and work in conjunction with the Grosberg and Zaragoza labs to try to match simulated nuclei to their patient and control samples. This will elucidate the mechanism by which nuclear blebs form in disease states, and further our understanding of the disease itself.

3. Cell surface mechanochemistry and the determinants of bleb formation, healing and travel velocity^{*}

3.1 Introduction

The eukaryotic cell surface is the site of cell-cell communication [3], cell-environment interactions including motility and mechanosensing [69], and cell morphogenesis [2], among other processes. Many of these processes involve mechanical forces and deformation, making mechanics of the cell surface an increasingly important topic of investigation.

The study of cell surface mechanics is complicated by dynamic interactions among its multiple constituents with distinct material properties. The plasma membrane is fluid [53] and resists deformation and experiences surface tension on the order of 10-100 pN/nm [62] that is spatially and temporally non-uniform [49]. Below the membrane is a ~ 100 nm layer of F-actin with distinct microarchitecture from the cytoplasmic F-actin further into the cell [16], termed the cortex. The cortex is anisotropic poro-viscoelastic material [56, 27] that generates internal active contractile stresses by association with myosin [62]. The membrane and cortex are decorated with a myriad of molecules, some of which interact with both of them, thereby facilitating dynamic adhesion between them [25]. This complexity obscures fundamental questions such as, how quickly is hydrostatic pressure propagated through the cortex [59, 14, 17], or surface tension propagated across the membrane [49, 23, 53]? These questions have functional consequences since, for example, membrane bending and tension are implicated in endocytosis [42], cell polarization [31] and motility [23?], while the cortex is implicated in cell division, initiating filopodia and other cellular protrusion [40], both facilitating and preventing vesicle export [63], and wound healing [56].

An example cell process that involves all the above components is offered by cellular blebbing, pressure-driven protrusions that occur in many cell types and conditions [12, 13, 47]. An individual bleb begins with an initiation phase whereupon the membrane separates from the cortex, either spontaneously or under experimental triggering such as laser ablation [16, 12]. Initiation is followed by a rapid (~ 10 s) expansion phase which, unlike other cellular protrusion, is not actively driven by cytoskeletal polymerization [18]. After expansion, blebs can exhibit a range of dynamic behaviors: Stationary blebs heal in place with a slower timescale (\sim minutes). Other classes of bleb that have been experimentally observed travel

K. Manakova[†], H.Yan[†], J. Lowengrub[†] and J. Allard^{†‡}

around the periphery of the cell — a phenomenon termed circus movement [26, 46, 41] — or repeatedly bleb on top of an existing bleb [12]. The complete life-cycle is determined by a complex interplay between flow of cytosol into the bleb, contractive forces in the cortex and the formation and maintenance of membrane-cortex adhesions. Blebs are implicated in non-lamellipodial cell motility [43, 11], including in protease-inhibited cancer cells [24]; in maintaining homeostasis during division [57]; and have a speculated role in the origin of eukaryotic life [4].

Traveling waves of protrusion are increasingly reported in different cell types [31, 55], but these protrusions are typically F-actin-enriched (although see [36]), whereas blebs represent regions with reduced F-actin. A fundamental question to the understanding of any traveling wave phenomenon [2] is: what determines the traveling velocity of a traveling bleb? And, in the case of blebs which may be stationary or travel, even simultaneously at different locations on the same cell, what determines whether a bleb will travel or heal in place?

Several theoretical models of blebbing have been developed to capture various aspects of the process. Computational fluid dynamics models [59, 58, 68] have been developed to understand the initial expansion phase during which cytosolic fluid follows the protruding membrane. Due to the computational cost of solving the fluid equations along with their mechanical interaction with immersed structures (which typically have sub-second dynamics [59, 58]), simulations of these models are typically limited to 2D approximation and seconds timescales. Other researchers [41] have used force-balance models [1, 36] to obtain computationally tractable models describing the full life cycle. These models are in 2D and must assume an *a priori* bleb healing velocity to generate traveling blebs. Continuum analytical models [65, 66, 64] have also been developed that move beyond the typical small-deformation approximations typically used to describe membrane geometry. These models capture details of the shape of stationary bleb that have, among other findings, implicated lipid flow in determining bleb behavior.

A full, 3D description of the full life-cycle of traveling blebs is therefore lacking. In this work, we develop a model of local cell surface mechanics on timescales of seconds to minutes, thereby including cortex turnover and bleb healing. We exploit two simplifying assumptions: First, we assume hydrodynamic equilibrium is reached rapidly and therefore avoid computationally taxing fluid dynamic simulation, at the expense of losing information about the expansion phase. Second, our model contains a single, “effective” cortex corresponding to the weighted average of cortical actin, allowing us to include implicitly the cytoskeleton further inside the cell.

An emerging feature of this model is that transient detachment between membrane and cortex can lead to: 1) rapid healing, 2) stationary bleb formation, and 3) spontaneous bleb travel, depending on model parameters. Our model makes two main contributions: First, since traveling blebs arise naturally, we can elucidate the determinants of bleb travel. In particular, several simplifying assumptions allow us to obtain an analytic expression for bleb travel velocity that provides experimentally-accessible perturbations predicted to accelerate or decelerate travel. Our second finding is that the biophysical ingredients hypothesized to account for blebbing produce traveling blebs with unrealistic geometry. This suggests yet-to-be-identified mechanism playing a role in cell integrity and the localization of morphological perturbations. We explore the influence of dynamic, non-uniform membrane tension; hydrostatic pressure equilibration occurring at multiple length scales (i.e., global versus local

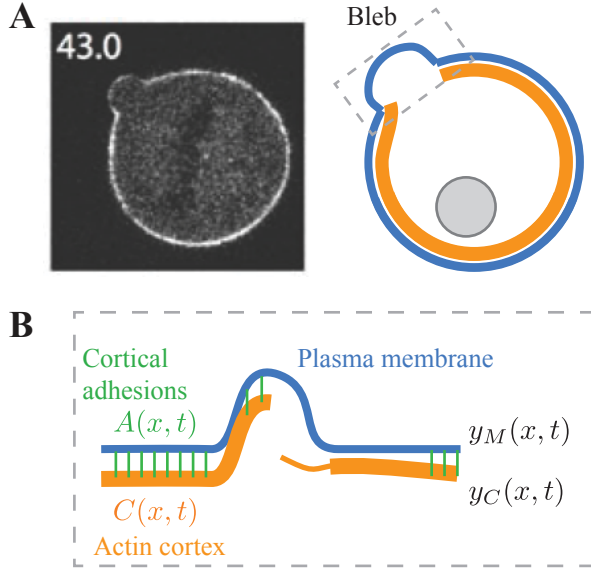


Figure 3.1: (A) Micrograph of a single bleb, induced by laser ablation on the surface of a HeLa cell, 43 seconds after initial formation. Taken from [6]. (B) Model components. At each location on the surface of the cell x , four quantities are represented: The height of the membrane $y_M(x, t)$, the height and thickness of the actin cortex $y_C(x, t)$ and $C(x, t)$ respectively, and the local density of membrane-cortex anchoring proteins, $A(x, t)$. Note that the schematic shows the range of possible model states (e.g., thick or thin cortex, protruding or proximal membrane), while specific predicted dynamics will be determined by simulation.

[58]); and spatial heterogeneity. We find the latter sufficient to maintain bleb compactness during travel.

3.2 Model

Our minimal model, summarized schematically in Fig. 3.1, consists of four fundamental dynamic variables, as functions of time t and location on the two-dimensional cell surface, parametrized by (x_1, x_2) . The actin cortex, has local height described by $y_C(x_1, x_2, t)$ measured normal to the mean cell surface from its steady-state configuration $y_C = 0$, and thickness $c(x_1, x_2, t)$. The cortical-cytoplasmic actin cytoskeleton can in principle have complicated morphologies that cannot be accounted for by a single location y_C , so we think of y_C as the weighted average position of maximal cortical actin. Membrane-cortex adhesions are described by density $a(x_1, x_2, t)$ in molecules/nm². Finally, the membrane has local height $y_M(x_1, x_2, t)$. Note that our model is agnostic about the molecular constituents of the membrane, and it could include the plasma membrane as well as permanently membrane-associated proteins and cytoskeletal networks [36]. Our approach is similar to previous descriptions of membrane mechanics [1, 41, 3, 49].

3.2.1 Assembly and turnover.

The cortex is an active, anisotropic poro-viscoelastic material [56, 27]. Since the molecular details of cortex assembly are still under investigation [7], we assume simple first-order kinetics,

$$\frac{\partial c}{\partial t} = \omega a - r c. \quad (3.1)$$

The first parameter ω governs cortex assembly, and assumes new cortex requires adhesion to a nearby membrane (although existing cortex can exist anywhere), consistent with the observation that cortical actin has different architecture than cytoplasmic F-actin [16]. The second term describes cortex turnover with rate $r \sim 0.05 \text{ s}^{-1}$ [25]. While we use the term thickness, we interpret c as a combination of density and spatial thickness, with fluorescence intensity of labelled F-actin serving as its experimental proxy. Therefore c has arbitrary units.

In stereotypical, pre-bleb conditions, the cortex is attached to the membrane via membrane-cortex adhesion molecules including ezrin- radixin- moesin (ERM) family proteins [25], as well as any other membrane proteins that interact with F-actin [48], therefore we use the generic term “adhesion” to describe their combined effect. We use similar first-order kinetics for adhesion assembly and turnover, with three additional assumptions: 1) Adhesion assembly saturates at high cortex thickness; 2) Adhesion attachment requires proximity between cortex and membrane, with characteristic distance δ that describes the “reach” of adhesion molecules, which may be as large as $\sim 100 \text{ nm}$ [16]; and 3) Adhesion detachment is force-dependent with characteristic breaking force f_0 . These assumptions lead to

$$\frac{\partial a}{\partial t} = \frac{k_{\text{on}} c}{c_0 + c} \exp\left(-\left(\frac{y_M - y_C}{\delta}\right)\right) - k_{\text{off}} a \exp\left(\frac{\kappa(y_M - y_C)}{f_0}\right) \quad (3.2)$$

where k_{on} and k_{off} have units of $\text{nm}^{-2} \text{ s}^{-1}$ and s^{-1} , respectively, and c_0 is the cortex thickness at which adhesion assembly is half-maximal. The numerator $\kappa(y_M - y_C)$ follows from the assumption that adhesions collectively behave like springs with Hookean stiffness κ . Note that adhesion turnover $k_{\text{off}} \sim 2 \text{ s}^{-1}$ [25] is significantly faster than cortex turnover, leading to a separation of timescales we exploit.

3.2.2 Mechanics.

The above equations describing assembly and disassembly kinetics are coupled to a mechanical description of the membrane and cortex via mechanical energy,

$$E = \iint \mathcal{H}_1 + \mathcal{H}_M + \mathcal{H}_C dx_1 dx_2 \quad (3.3)$$

where

$$\mathcal{H}_1 = \frac{1}{2} a \kappa (y_M - y_C)^2 - \Pi. \quad (3.4)$$

The first term corresponds to tension on the adhesions. Since these adhesions break at moderate tension, we model these as linear springs. The second term is hydrostatic pressure Π , specified below. Membrane mechanics are described by

$$\mathcal{H}_M = \frac{1}{2} \gamma_M (\nabla y_M)^2 + \frac{1}{2} B_M (\nabla^2 y_M)^2 \quad (3.5)$$

corresponding to the standard Canham-Helfrich energy with membrane tension γ_M and bending rigidity B_M [29, 1, 66, 41]. These functional forms represent a small-deformation approximation and comprise a simplifying assumption to make the model more easily amenable to the analysis. We therefore do not expect our model to capture the shape of a fully-expanded bleb with high accuracy, for which geometrically more complex models have been developed [64]. Finally, mechanics of the actin-myosin cytoskeleton is included in

$$\mathcal{H}_C = c\sigma_m \left(y_C^2 + \frac{1}{2} w_C (\nabla y_C)^2 \right), \quad (3.6)$$

accounting for active of the cortex, which generates contraction stress $\sigma_m c$, assumed proportional to cortex thickness. The first term accounts for inward contractility, as the cortical cytoskeleton pulls against the cytoplasmic cytoskeleton, generating a normal (inwards) force, as shown in Fig. A.1. Note this term has been neglected in previous work [41]. The second term accounts for tangential stress in the plane of the cortex, where w_C is the cortex dimension that translates the 3D contractile stress to a tangential planar contractile tension. Importantly, we find that in traveling blebs, where the cortex is discontinuous, the tangential term does not generate sufficient inward force to heal the tail of the bleb as it travels, highlighting the importance of the normal contractility term. Cortex elasticity terms describing how the cortex resists deformation are straightforward to add, however we find that their omission is sufficient to explain our key results.

The mechanical features included in the energy Eq. 3.3 can also be understood by their equivalent force-balance form, Eq. 3.8-3.9 below.

Pressure propagation inside the complex rheology of the cytoplasm is under intense investigation [15, 59, 57]. To address the nature of pressure dynamics, we investigate several pressure model variants. As a base model, we assume pressure is locally relaxed when the membrane is allowed to relax,

$$\Pi = \hat{\Pi} \cdot \left(1 - \frac{y_M}{2y_M^0} \right)^2 \quad (3.7)$$

where y_M^0 sets the characteristic distance at which pressure is significantly reduced. The pressure drop would be lessened if the membrane is locally water-permeable [?], which would have the effect of reducing the coefficient relating pressure to membrane extrusion. Other model variants explore the possibility of rapidly-equilibrated pressure across the whole cell surface and a mixture of global and local pressure relaxation.

The dynamics of membrane tension are also under investigation [23, 51, 62, 31, 2]. Under the simplest assumption, membrane tension γ_M is spatially uniform and constant in time. We use this as our base model, but also explore membrane tension that is spatially non-

Table 3.1: Model parameters.

Symbol	Dimensions	Meaning
ω	[A.U.] $\cdot s^{-1}$	Cortex assembly rate constant
r	s^{-1}	Cortex turnover rate constant
k_{on}	$nm^{-2} s^{-1}$	Adhesion assembly rate
k_{off}	s^{-1}	Adhesion turnover rate
c_0	[A.U.]	Cortex thickness at adhesion saturation
δ	nm	Adhesion length between cortex and membrane
κ	pN/nm	Adhesion spring constant
f_0	pN	Adhesion breaking strength
γ_M	pN/nm	Membrane tension
B_M	pN nm	Membrane bending modulus
σ_m	Pa / [A.U.]	Actin-myosin contractility (per unit of c)
$\hat{\Pi}$	Pa/nm	Hydrostatic pressure scale

uniform and dynamically responding to local stretching/unruffling and cortex attachment in Results.

3.2.3 Preliminary analysis.

Taking the variational derivative of Eq. 3.3 leads to force-balance equations on the cortex and membrane,

$$0 = +a\kappa(y_M - y_C) - \sigma_m c y_C + \sigma_m c w_C \nabla^2 y_C \quad (3.8)$$

$$0 = -a\kappa(y_M - y_C) + \frac{\delta \hat{\Pi}}{\delta y_M} + \gamma_M \nabla^2 y_M - \beta \nabla^4 y_M \quad (3.9)$$

Physical parameters are summarized in Table 3.1. Values for many of these parameters have been estimated, see Fig. A.1. The spatial terms significantly complicate both numerical solution and analysis of the model, and we find that their omission does not significantly influence blebbing dynamics. This is expected for membrane bending, since bending forces are expected to be negligible on length scales above $\sim (\beta/\gamma_M)^{(1/4)} \sim 100$ nm [3]. Therefore, unless otherwise noted below, we neglect the tangential cortex stress $\nabla^2 y_C$ and membrane bending $\nabla^4 y_M$ terms. However, see Appendix A.1 for solutions with full terms.

We non-dimensionalize by choosing a characteristic actin cortex thickness, $C_c = c_0$, a characteristic density of adhesions, $A_c = k_{on}/k_{off}$, a characteristic time, $t_c = 1/r \sim 30$ s [25], and a characteristic position, $Y_c = y_M^0$, and a characteristic length by $x_c =$

Table 3.2: Non-dimensional parameters.

Symbol	Definition	Interpretation
Ω	$\omega k_{\text{on}}/\gamma c_0 k_{\text{off}}$	Cortex intensity
ϵ	r/k_{off}	Ratio of adhesion and cortex turnover times
D	δ/y_M^0	Adhesion reach
F_0	$f_0/\kappa y_M^0$	Adhesion bond strength
M	$\sigma_m c_0 k_{\text{off}}/k_{\text{on}} \kappa$	Myosin contractility relative to adhesion strength
P	$\hat{\Pi} k_{\text{off}}/k_{\text{on}} \kappa$	Pressure relative to adhesion strength

$\sqrt{2\gamma_M k_{\text{off}}/(k_{\text{on}} \kappa)} \sim 0.2 \mu\text{m}$, resulting in a non-dimensional model,

$$\frac{dC}{d\tau} = \Omega A - C \quad (3.10)$$

$$\epsilon \frac{dA}{d\tau} = \frac{C}{1+C} \exp\left(-\frac{Y_M - Y_C}{D}\right) - A \exp\left(\frac{Y_M - Y_C}{F_0}\right) \quad (3.11)$$

$$0 = A(Y_M - Y_C) - MCY_C \quad (3.12)$$

$$0 = -A(Y_M - Y_C) + P(1 - Y_M) + \frac{\partial^2 Y_M}{\partial \chi^2} \quad (3.13)$$

with six nondimensional parameters defined in Table 2.

Here we provide an overview of the roles of each term in Eq. 3.10-3.13. The first and second term in the C equation describe cortex formation and turnover, respectively. The first and second term in the A equation describe attachment and detachment of cortex-membrane adhesions. The first exponential in Eq. 3.11 arises because the membrane and cortex must be in proximity for an adhesion to form. The second exponential in Eq. 3.11 describes the accelerated breaking of adhesions under force. Then, Eqs. 3.12 and 3.13 describe the mechanical balance between five forces acting on the membrane and cortex. The forces, in order of appearance, are: Adhesion force on the cortex; myosin contractility of the cortex; adhesion force on the membrane; pressure; and membrane tension.

Note that our choice of nondimensionalization means that only relative changes in Y_M and Y_C are physically meaningful. We numerically solve these equations as described in Appendix A.1 [?].

3.3 Results

3.3.1 Model exhibits blebbing and non-blebbing behaviors.

The quantitative model combines five mechanisms of the membrane-cortex interaction: force-sensitive adhesions, local hydrostatic pressure, cortex contractility, membrane tension and cortex turnover. We numerically simulate the model and find three classes of dynamics arise from the same model at different parameters: Stable non-blebbing states, stationary blebbing, and traveling blebs. We discuss these in turn.

At equilibrium, the membrane and cortex are locally approximately flat. We apply an

initial perturbation corresponding to local ablation by locally reducing the adhesion density by 99%. In blebbing states, the membrane will detach from the cortex and protrude locally. The membrane then continues to move away from the thinning cortex as the detached region grows in both lateral size (along the surface) and in height (i.e., normal to the cell surface) until it reaches a maximum size around $\tau = 1.75$. The adhesions subsequently accumulate under the protruding membrane and the cortex is able to re-attach and thicken. Under the influence of cortex contraction, the bleb heals and the membrane returns to its equilibrium. This bleb-like behavior is observed in 2D (Fig. 3.2A left) and in 3D (Fig. 3.2B) simulations. In contrast, at different biophysical parameters, the detached region of membrane may not grow after perturbation, but instead directly and rapidly return to equilibrium, shown in Fig. 3.2A right. This stable behavior is observed in both 2D (Fig. 3.2A right) and in 3D (not shown).

3.3.2 Blebs as excitable phenomena

While numerical simulation of the full model reveals a range of blebbing behavior, we seek to elucidate how biophysical parameters determine the class of dynamics, specifically whether or not a bleb forms. To this end, we simplify the model by neglecting the tension term in Eq. 3.12. Heuristically, we model an (unrealistic) system in which a patch of cell surface has been cut off from its neighbors (as in Fig. A.1). This transforms the force-balance equations Eq. 3.12-3.13 into a pair of algebraic equations,

$$Y_M = \frac{(A + CM)P}{AMC + AP + MCP} \quad (3.14)$$

$$Y_C = \frac{AP}{AMC + AP + MCP}, \quad (3.15)$$

shown in Fig. 3.3A as a function of A and C . These are then substituted into the assembly/disassembly equations, yielding

$$\frac{dC}{d\tau} = \Omega A - C \quad (3.16)$$

$$\epsilon \frac{dA}{d\tau} = \frac{C}{1+C} \exp \left(-\frac{1}{D} \frac{MPC}{AMC + AP + MCP} \right) - A \exp \left(+\frac{1}{F_0} \frac{MPC}{AMC + AP + MCP} \right) \quad (3.17)$$

The model is now a system of two ordinary differential equations (ODEs) amenable to phase plane analysis [21]. We plot nullclines in which $dA/d\tau = 0$ (green) or $dC/d\tau = 0$ (orange) in Fig. 3.3B,D. Four regimes of behavior are observed in this system: In one (top-left), there is a single stable equilibrium with no threshold behavior. In this regime, perturbations rapidly return to their steady state. We identify this with the stable non-blebbing behavior of the full model.

The stable equilibrium can exhibit excitability (bottom-left), a threshold phenomenon in which small perturbations rapidly return to the equilibrium, but a large sufficiently large

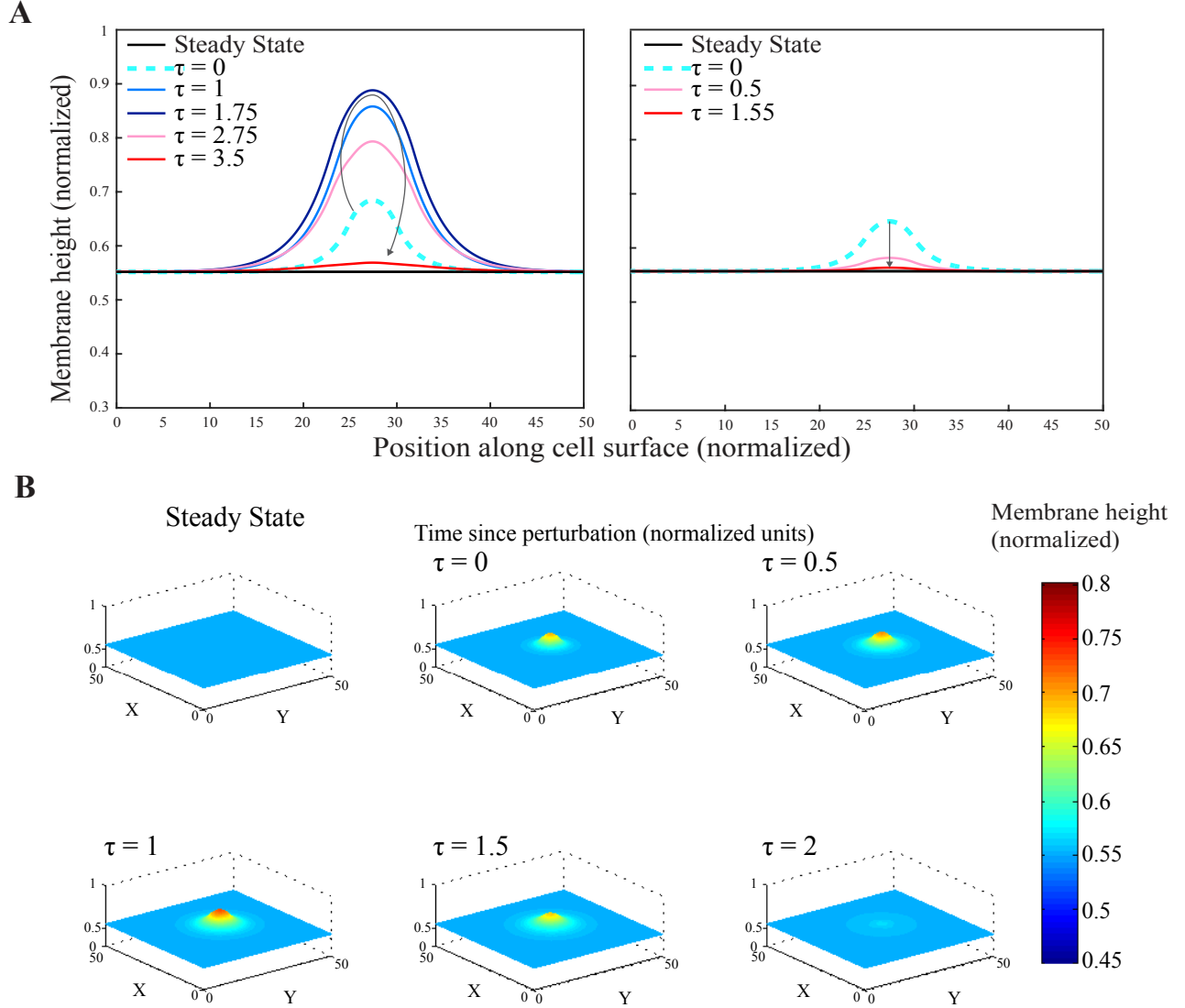


Figure 3.2: Model exhibits stationary blebs and non-blebbing states in 2D and 3D. (A) Profile of stationary solution of the 2D system: (Left) Excitable state in which an initial perturbation (cyan dashed) expands in both height (normal to cell surface) and laterally along cell surface before retracting. (Right) Non-excitable state in which the initial perturbation rapidly and directly returns to equilibrium. Parameter values: $\Omega = 40$, $\epsilon = 0.1$, $F_0 = 1$, $M = 0.007$, $P = 0.1$ and $D = 0.15$ for the excitable state, $D = 0.2$ for the non-excitable state. (B) Profile of stationary solution of the 3D system in an excitable state. Parameter values: $\Omega = 50$, $\epsilon = 0.1$, $F_0 = 1$, $M = 0.007$, $P = 0.1$ and $D = 0.15$. Note that our choice of nondimensionalization means that only relative changes in Y_M and Y_C are physically meaningful.

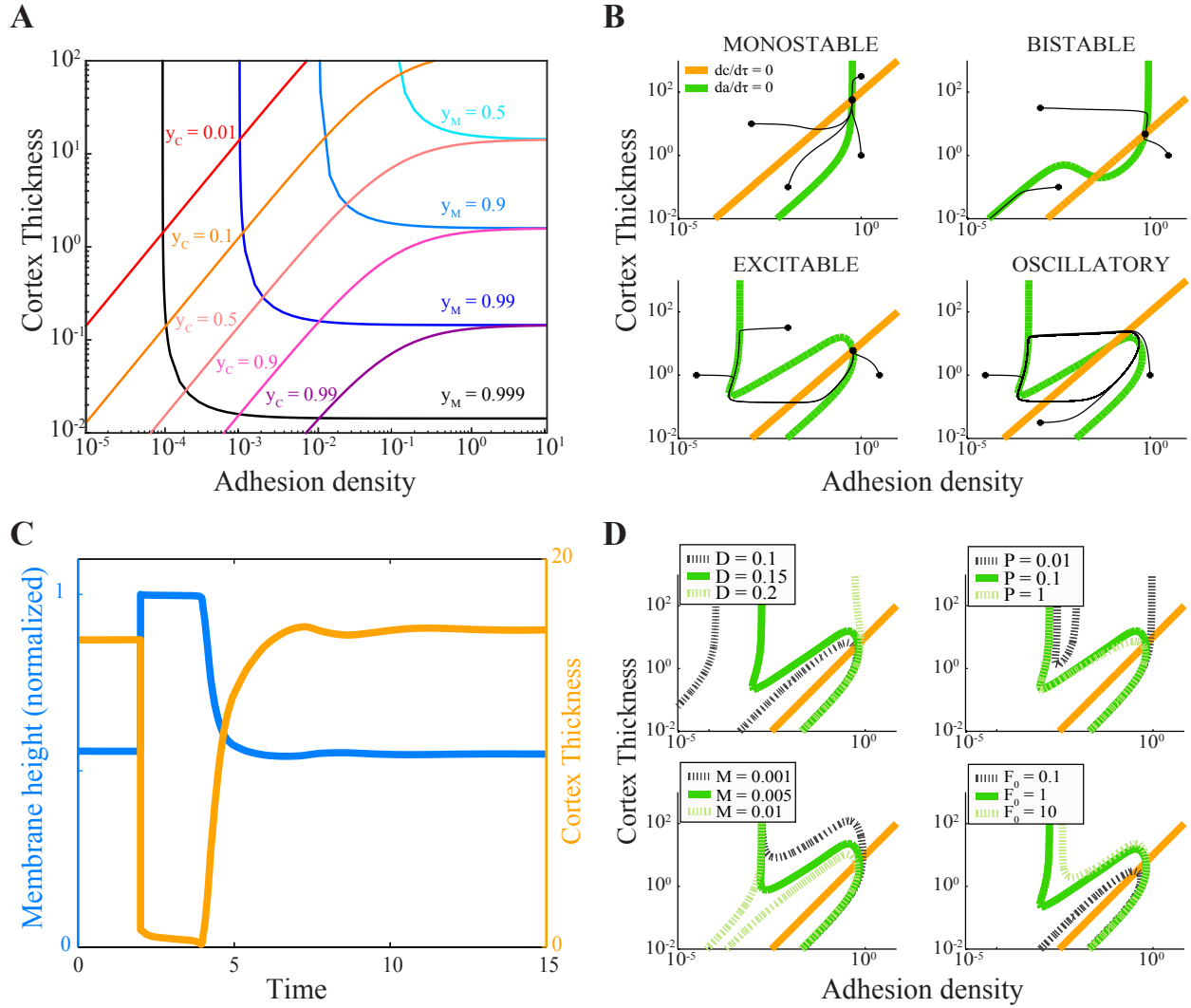


Figure 3.3: Emergence of blebbing states can be understood in terms of the local $A - C$ phase plane. (A) Since the model assumed force-balance between adhesions, cortex and membrane, a particular value of A and C determine the current position of the membrane and cortex y_M and y_C via Eq. 3.14-3.15. (B) Range of behaviors of the system of equations given different parameter sets visualized by the nullclines (orange for C and green for A) of the non-dimensionalized system of equations, Eq. 3.17-3.16. Sample trajectories are shown in black. Monostable parameters: $\Omega = 100$, $\epsilon = 0.1$, $F_0 = 6.3$, $M = 0.09$, $P = 0.08$ and $D = 0.23$. Bistable parameters: $\Omega = 6.5$, $\epsilon = 0.1$, $F_0 = 2.9$, $M = 0.43$, $P = 0.016$ and $D = 0.19$. Oscillatory parameters: $\Omega = 100$, $\epsilon = 0.1$, $F_0 = 1$, $M = 0.007$, $P = 0.1$ and $D = 0.15$. Excitable parameters: $\Omega = 10$, $\epsilon = 0.1$, $F_0 = 1$, $M = 0.007$, $P = 0.1$ and $D = 0.15$. (C) Time series plot of membrane position (blue) and cortex thickness (orange) beginning in steady state, with a perturbation at time $\tau = 2.5$. (D) The effect of parameter variation on the nullclines. Parameters which are not being varied as indicated in legend are fixed as: $\Omega = 10$, $\epsilon = 0.1$, $F_0 = 1$, $M = 0.007$, $P = 0.1$ and $D = 0.15$.

perturbation results in a large, slow excursion in parameter space that eventually returns to the equilibrium. We identify this with blebbing behavior in the full model and is characterized by a fold in the $dA/d\tau$ nullcline.

One such excitation trajectory is shown in Fig. 3.3C. Prior to the initial perturbation, $\tau < 2$, the flat surface is stable to small perturbations but susceptible to large perturbations such as the decrease in adhesion density applied here at $\tau = 2$. The membrane rapidly finds a new mechanical equilibrium, pushed out by hydrostatic pressure which is no longer in competition with cortical contraction. The comparatively slow timescale of cortical turnover (orange curve) leads to a delay before cortex begins to reform ($\tau \approx 4$), after which the cortex accumulates, pulling in the membrane. Note that many excitable trajectories exhibit low-amplitude oscillations in the cortex as it heals, corresponding to a slight “over-shooting” of the equilibrium ($\tau \approx 7$). Interestingly, such overshooting has been observed experimentally [16].

The minimum threshold to initiate an excitation can be extracted from Fig. 3.3 as follows: The stable equilibrium is at the intersection of the two nullclines. From this point, removing adhesions corresponds to moving horizontally to the left. When adhesion removal is sufficient to cross the $dA/d\tau$ nullcline, an excitation is initiated. Since the $dA/d\tau$ nullcline determines this threshold, it is independent of membrane tension. This is in disagreement with previous estimates of the threshold, where membrane tension has been predicted to be a strong determinant of the size of initial ablation required for bleb initiation [13]. In contrast, our model predicts that membrane tension determines how big a bleb grows (laterally), but not whether it initially grows. This tension-independence arises heuristically because, once a patch of membrane has been de-adhered, membrane tension promotes bleb growth by pulling neighboring adhesions, and inhibits bleb growth by pulling in the de-adhered region. By the force-balance condition (Eq. 3.9), these forces are equal.

We also observe oscillations (bottom-right), which could represent continually blebbing cells [12]. At yet other parameters, the same model exhibits bistable states (top-right) in which the flat, unperturbed equilibrium is stable, but is accompanied by a second state in which all adhesions are broken, and hydrostatic pressure is too great for the actin cortex to overcome, thus healing does not spontaneously occur. We expect this permanently-damaged state to not be observed experimentally as other cellular processes adjust to heal the cortex.

Thus, by observing the nullclines for different parameters, our model makes predictions about the emergence of blebbing following changes in biophysical parameters (Fig. 3.3D). We summarize these predictions here and in Table A.1. Increasing the effective reach of adhesion molecules corresponds to increasing D , and abolishes excitability, while decreasing D is predicted to not abolish blebbing but extends the excitable trajectory, therefore predicting a slower healing period. Increasing hydrostatic pressure, e.g., by decreasing extracellular pressure by modulating osmolites, leads to emergence of blebbing from non-blebbing states, in agreement with experiment [62] and intuition. Decreasing myosin contractility abolished excitability, while increasing it delays healing.

3.3.3 Biophysical determinants of travel and travel velocity

The previous section’s analysis predicts when the cell surface will be excitable and how the bleb evolves in height, but not its dynamics along the cell surface. To understand bleb travel,

we return to the full, spatially-extended model first in 2D, then in 3D.

Excitable parameter sets all spread laterally. However, some parameter sets expand in a limited manner (Fig. 3.2A), which we identify as stationary blebs, while others trigger traveling pulses that persists, as shown in Fig. 3.4A. We identify these as traveling blebs. In 2D, they move in both directions from the site of initial triggering. The time interval τ_{heal} from triggering and expansion to healing is equal to the healing time in the local analysis and is determined by the cortex turnover time $\tau_{\text{heal}} \sim 1/r$. The width of the traveling bleb w is thus determined by its travel velocity, $w \sim v\tau_{\text{heal}}$.

Traveling pulses are a generic feature of spatially-extended excitable systems [35, 54, 5]. In many cases, neighboring regions are coupled by the diffusion of a molecular participant. In these reaction-diffusion systems, a simple mathematical condition exists for determining whether an excitation will induce a traveling pulse or remain localized, sometimes called the Maxwell condition [8, 44]. Since our system is not a reaction-diffusion system, the Maxwell condition fails to predict whether the blebs travel or not.

A major goal of this work is to elucidate the determinants of the traveling velocity, which is known for reaction-diffusion waves and mechanical linear waves [2]. Parameter variations, shown in Fig. 3.5, reveal that the parameter regime that allows traveling blebs is narrow in all non-dimensional parameters except ϵ . Indeed, its relative range is less than $10^{0.3}$, corresponding to a 2-fold change. The model therefore predicts a non-dimensional velocity $V \sim 1/\epsilon$, yielding the following dimensional velocity, the principle result of this work:

$$v \approx \sqrt{\frac{\gamma_M k_{\text{off}}^3}{\kappa k_{\text{on}}}} h(\Omega, D, F_0, P, M) \quad (3.18)$$

$$\approx \sqrt{\frac{\gamma_M k_{\text{off}}^3}{\kappa k_{\text{on}}}} \quad (3.19)$$

where the function h expresses to a weak dependence. We confirm this prediction in Fig. 3.5B by performing a large pan-parametric search through parameter space. Eq. 3.19 predicts that travel will accelerate with increasing membrane tension, with a specifically square-root dependence, and will decelerate with adhesion formation rate k_{on} , a parameter that could be varied by increasing the abundance of total adhesion molecules. The affinity of adhesions for the cortex, $K_A \equiv k_{\text{on}}/k_{\text{off}}$, is also predicted to have a decelerating influence on bleb travel. Interestingly, all other parameters, including hydrostatic pressure and myosin contractility, are predicted to have only a minor influence on travel velocity. Note, however, that these parameters strongly determine whether or not a bleb can form, and whether or not the bleb travels laterally. This model prediction is distinct from a previous prediction [41], which posited that cortex healing has an intrinsic velocity, and that this velocity determines bleb travel velocity.

3.3.4 Hypotheses for compact traveling blebs

In 3D, the base model also exhibits excitations that either travel or heal in place, in agreement with the local analysis and 2D model. Parameter conditions for excitability and travel are the same as for the 2D model, as is travel velocity. However, we find that a localized

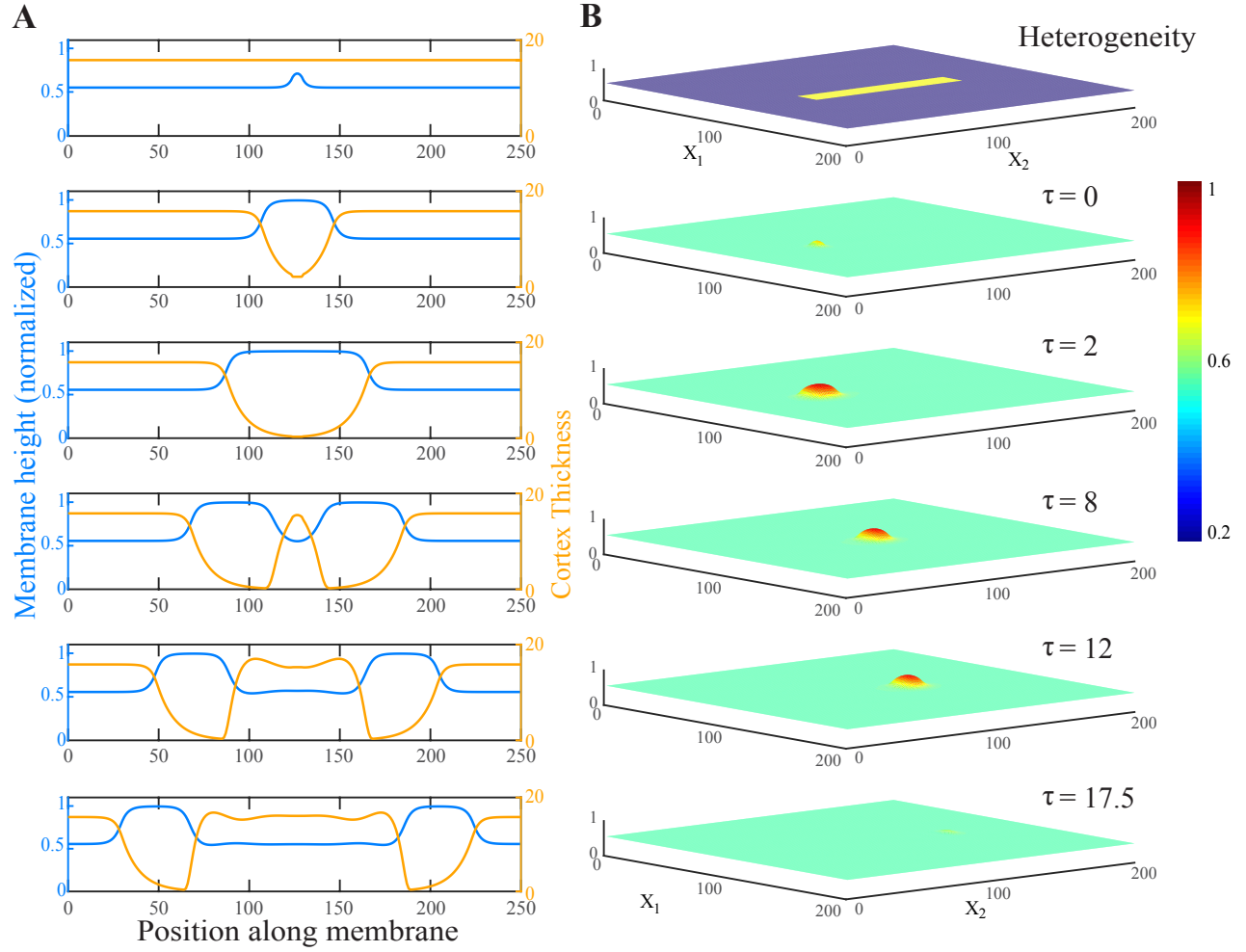


Figure 3.4: Traveling blebs in 2D and 3D. (A) Profile of a traveling blebs in 2D after a perturbation at time $\tau = 0$. Membrane height in blue, cortex thickness in orange. Parameter values: $\Omega = 55$, $\epsilon = 0.1$, $F_0 = 1$, $M = 0.007$, $P = 0.1$ and $D = 0.15$. (B) Profile of a traveling bleb in 3D after a perturbation at time $\tau = 0$ in the spatial-heterogeneity hypothesis model as shown in top panel, see Results.

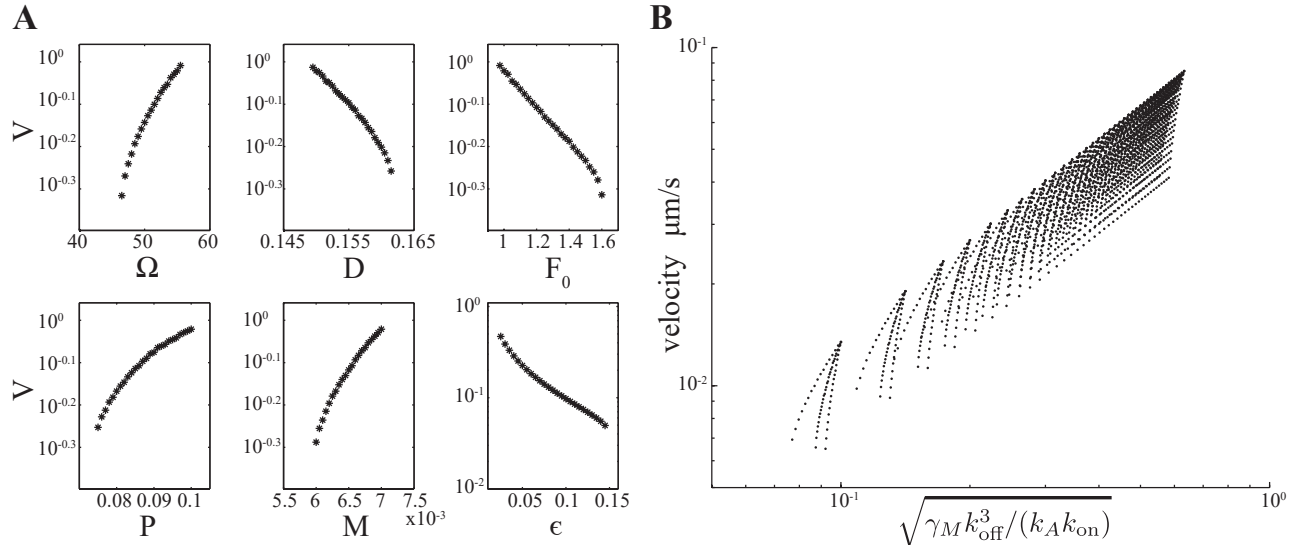


Figure 3.5: Velocity of traveling blebs. A) Plot of each of the 6 non-dimensional parameters, Ω , D , F_0 , P , M , ϵ , versus non-dimensional velocity. Parameter ranges show the full extent of the parameter regime exhibiting traveling solutions. Fixed parameters in each plot are: $\Omega = 55$, $\epsilon = 0.1$, $F_0 = 1$, $M = 0.007$, $P = 0.1$ and $D = 0.15$. (B) Plot of hypothesized relationship between velocity, Eq. 3.19, versus velocity observed in numerical simulation.

initial perturbation spreads radially in all directions, leading to an expanding bull's-eye or target pattern, Fig. 3.6B. This is a generic feature of excitable systems and arises because of inherent symmetry: a protruding region of membrane will pull neighboring regions of membrane, without directional bias.

Since traveling blebs are not experimentally observed to expand in bull's eye patterns, we are led to investigate the question of what gives rise to spatially compact traveling blebs? That is, what breaks the symmetry, inducing travel in a single direction?

We introduce three hypotheses. The first is that hydrostatic pressure may be reduced globally fast enough that, once the excited region enlarges past a certain size, there is no longer sufficient pressure to drive further excitation, thus limiting the target pattern to a compact region. In our model, we modify the membrane force-balance equation, Eq. 3.9, by including the pressure term

$$\Pi = \hat{\Pi} \cdot \iint \left(1 - \frac{y_M}{2y_M^0} \right) dx_1 dx_2. \quad (3.20)$$

This equation corresponds to a shared, global pressure that responds to pressure release (via membrane protrusion) instantly anywhere in the domain. We variously simulated purely global pressure, purely local pressure, and pressure with both local and global equilibration, following recent theoretical evidence [60].

We find that global pressure dynamics can limit the bleb's outward growth when $\hat{\Pi}$ is sufficiently large. However, we do not see symmetry breaking, even upon introduction of 10%

parametric noise (Fig. 3.6A). Interestingly, at intermediate global pressures, the bleb does not heal and instead undergoes slow oscillations (Fig. 3.6A right). These oscillations reveal an inherent negative feedback between cortical formation, which builds pressure, which in turn breaks adhesions, weakening the cortex.

The second hypothesis is that bleb compactness and asymmetry is due to a dynamic, non-uniform membrane tension. Following recent evidence [51], we introduce the assumption that tension increases with increasing local cortical actin contractility,

$$\gamma_M = \gamma_{M0} + \gamma_{M1}C. \quad (3.21)$$

We find that this is sufficient to terminate the protrusion (Fig. 3.6B), but, again, do not observe symmetry breaking.

Our third hypothesis is that large-length-scale heterogeneity, specifically on the \sim micron length scale of blebs, exists in the local density of proteins such as adhesion molecules and cortical actin nucleators. These manifest as spatial heterogeneity in model parameters such as D and Ω . Since these parameters sensitively determine whether the bleb can travel, such heterogeneity might create specific paths, forcing traveling blebs from spreading in all directions. We simulate the model on a surface in which a small rectangular region has distinct parameters from its surrounding region, as shown in Fig. 3.4B top. Since the parameter region allowing traveling blebs is fairly narrow (Fig. 3.5), it is straightforward to find parameter sets with less than 2-fold variation for which the equilibrium is the same, but only one allows travel. As expected, blebs initiated in the excitable-travel region remain compact and move with velocity v from Eq. 3.19, and front-to-back width $w \sim v\tau_{\text{heal}}$.

We conclude that small differences across large length scales in the underlying biophysical properties of the cell surface are sufficient to explain compact traveling blebs. This hypothesis makes the prediction that subsequent traveling blebs will tend to occur in the same location on the cell surface, provided that the heterogeneity's own timescale of variation is longer than the bleb lifetime.

3.4 Discussion

Excitability is a recurrent theme in cell biology [33, 67, 22, 5]. We find that the conditions for excitability emerge naturally from the mechanical properties of the cell surface, namely: the combination of a contractile cortex, a membrane exposed to internal hydrostatic pressure, and force-sensitive adhesions connecting them. In addition, membrane mechanical properties (i.e. surface tension) are sufficient for this excitability to lead to either limited-growth stationary blebs that heal in place, or traveling blebs reminiscent of circus movement. Notably, three classes of dynamics arise from the same model at different parameters: Stable, non-blebbing states (Fig. 3.2B), stationary blebbing (Fig. 3.2A,C); and traveling blebs (Fig. 3.4A,B). Thus our model provides quantitative conditions for bleb growth and whether the bleb heals locally or travels.

The model makes two main contributions. First, it allows elucidation of the determinants of the travel velocity in terms of biophysical parameters such as membrane tension and adhesion kinetics, Eq. 3.19. Surprisingly, we find that hydrostatic pressure and myosin

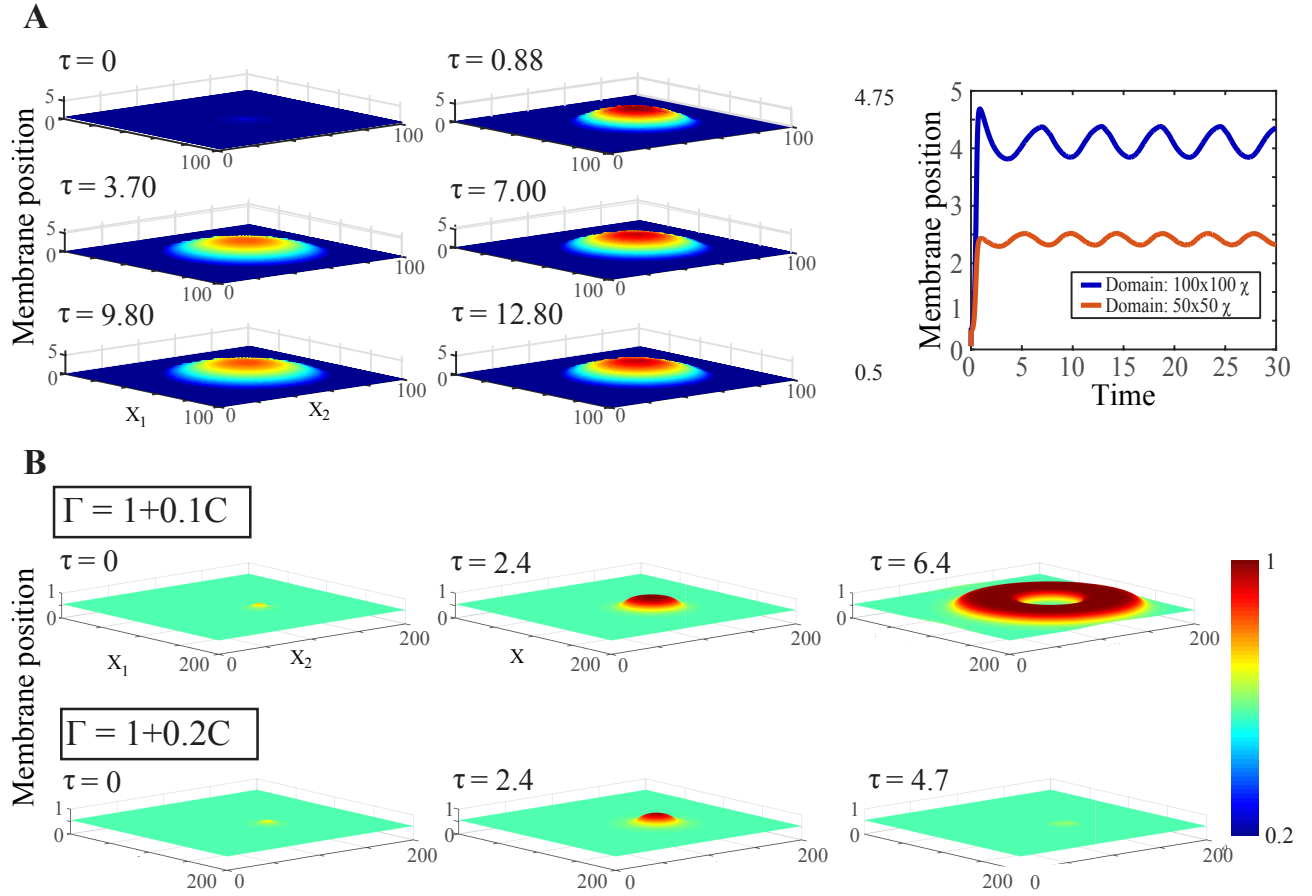


Figure 3.6: Alternative hypotheses for hydrostatic pressure and membrane tension dynamics. (A) Profile of 3D bleb using the global pressure model, Eq. 3.20, which assumes pressure equilibrates instantaneously across the domain. The bleb expands and contracts in oscillatory cycles (right panel). (B) Profile of a 3D bleb using a non-uniform tension model, Eq. 3.21, which assumes membrane tension depends on to the cortex thickness at a given point on the membrane. As the strength of this dependence increases (bottom row), the bleb no longer travels across the membrane. Here, $\Gamma = \gamma/\gamma_0$ is the non-dimensionalized membrane tension.

contractility only weakly determine velocity, while strongly determining other features such as whether the bleb forms, and its height. This is in distinction to previous assumptions [41] and other traveling waves in biology [2].

Our second finding is that known biophysical mechanisms are insufficient to account for the compactness of traveling blebs in 3D. The excitability inherent in the system leads to traveling waves. However, a striking distinction from other excitable waves on a two dimensional domain is that other waves create bull's eye patterns or spiral patterns. Since local membrane-cortex detachment promotes nearby detachment symmetrically, why do blebs travel in a compact shape, rather than spreading in all directions? Generically, for a shape to remain approximately constant as it travels, the normal velocity on its perimeter must vary from maximal at its front to zero at its sides. This observation, termed the Graded Radial Extension condition [39], was stated for steady cell motility but holds in general and therefore must be true for compact traveling blebs. One hypothesis we find sufficient to maintain compact travel is heterogeneity in the biophysical properties of the cell surface, such as adhesion density. There is no direct evidence that such heterogeneity is responsible for determining bleb travel paths, and it is likely that other mechanisms can explain compact travel. Since membrane tension is a strong determinant of local expansion velocity, it is possible that a model including different non-uniform membrane tension can recover a compact bleb in the absence of parametric heterogeneity. Other alternatives are: constraints set by lipid flow through the neck of the bleb [53], or nematic ordering in the cortex [36], which would break isotropic symmetry. For cells adhered to a rigid surface, the curvature is higher at the cell perimeter. This higher curvature could also potentially bias bleb formation and travel. We anticipate these will be a future direction of research.

A crucial feature of our model is the presence of a normal stress generated by the cortex, in addition to tangential stresses. We find that this normal stress is necessary for the dynamic healing and retraction of a traveling bleb. If myosin in the cortex generates an isotropic contractile stress, then it will induce stress in any direction in which there is F-actin. There is significant F-actin beneath the cortex (around 60% of the density in the cortex [? 16]), which is referred to as the cytoplasmic actin network and plays a role in cell integrity [?]. Our results suggest it also plays a role in retracting cellular protrusions.

The rheology of the cytoplasm, which determines how pressure propagates, is under intense investigation. Our model assumes a particular relationship between pressure change and volume change. To be as faithful to the correct rheology as possible, in the Results we simulate two extremes. Either (1) pressure relaxes entirely locally, with pressure at nearby locations unchanged, except perhaps on longer timescales if the bleb doesn't retract, i.e., pressure is local on short timescales, as described by our model Eq. 3.7. Or, (2) pressure relaxation spreads rapidly, and it nearly equal everywhere following blebbing, i.e., pressure is global on short timescales, as described by our model Eq. 3.20. Recent computational models of detailed cell rheology [60] demonstrate a more complicated possibility. Assuming the cytoplasm is poroelastic [14?], they find that, following blebbing, there is a small global drop in pressure, but full global equilibration is significantly slower. In the language of our model, this means that, on the $\sim 1\text{ s} - 10\text{ s}$ timescale we consider, part of the pressure drop is local and part is global. We may therefore be interested in a part-local, part-global pressure model. In Appendix A.1, we consider pressure models in which local membrane protrusion leads to both local and global pressure drops. We find that pressure must be at

least partly local, i.e., that neighboring regions are not equilibrated as quickly as at the site of protrusion, for blebbing to arise. As the global pressure drop is increased (corresponding to the assumption that the cytoplasm is less poroelastic and more like an incompressible fluid), the simulation approaches the purely global pressure model shown in Fig. 3.6A.

Increasingly, mechanics is included in theoretical models of cellular processes [48, 61, 49, 19, 52]. In these cases and others, subcellular mechanics equilibrates on sub-second timescales but drives processes that play out over seconds or slower, therefore mechanics is included via instantaneous force-balance or, equivalently, minimization of an energy functional as in Eq. 3.3 at every moment in time. Instead of reaction-transport (diffusion or advection) partial differential equations, these models can be expressed as a boundary value problem at each moment in time coupled to local time-dependent governing equations. This distinct class of models presents new opportunity for mathematical development. For excitable reaction-diffusion systems, a straightforward condition termed the Maxwell Condition [44, 8, 45] can be computed that determines whether the excitation will generate traveling waves. Analogous conditions for the new class of mechanical models may exist, and will be the subject of future research.

Our model makes several testable predictions about how bleb behavior will be modulated by experimental perturbations. The specific predictions about bleb formation and travel velocity, in Results, correspond to changes in hydrostatic pressure, which can be modulated via the extracellular pressure by, e.g., osmolites; Cortical turnover, which can be promoted or slowed by jasplakinolide or cytochalasin-D [16, 57]; Myosin contractility, which in blebs has been demonstrated to be susceptible to blebbistatin and indirectly to Y-compound [62]. In addition to these experiments, our model predicts that the “reach” of the adhesion molecules, δ , influences bleb characteristics via the (non-dimensional parameter D). It might be possible to modulate this parameter by mutagenically elongating or truncating cortex-membrane adhesion molecules.

In addition to the model variants we explored here, this model is readily extendible to different surface geometries and assumptions about stresses below and above the cell surface. An intriguing direction of research is the coupling of the present model of surface mechanochemistry with different rheological models of how stress evolves inside the cell [60, 14]. Another direction is the coupling to extracellular fluid dynamics, which have recently been proposed to play a role in determining membrane dynamics, even on slow (~ 1 s) timescales [10].

This work has been published in Biophysical Journal [Manakova et al. *Cell surface mechanochemistry and the determinants of bleb formation, healing, and travel velocity*. Biophys J, 110 (2016), pp. 1636-1647].

4. Analysis of traveling waves in a non-local model of cell surface mechanics

4.1 Introduction

The diffusion equation is used to described many scientific phenomena for decades and is very important to systems biology, in particular with respect to pattern development and the emergence of periodic structures from non-periodic sources during embryogenesis [37]. Because of it's long history and extensive applications, mathematical studies have revealed the conditions for various patterns to arise. The inclusion of biomechanics to chemical kinetic frameworks naturally leads to non-diffusion like PDEs. Here we will show that our model used to study cellular blebbing behavior (see Chapter 3) falls into this category. We believe a broad class of cellular behaviors obey similar mechanical constraints in conjunction with chemical dynamics, and therefore a study of the properties of these types of equations is a promising endeavor, and we plan to do a thorough literature review as part of our future work to identify such systems. In particular, we have chosen to investigate the conditions allowing for travelling wave solutions of a particular class of equations arising in cellular biophysics, a property already established in reaction-diffusion systems and sometimes called the Maxwell condition [8, 44]. We seek an analog of the Maxwell condition for the bleb model, and similar non-local PDEs. We will use our previously described cellular blebbing model as a test case.

4.2 ODE Analysis

The ODE system obtained by removing the spatial term in Equation 3.12 from our cellular bleb model of the previous section can exhibit a variety of behaviours numerically (Fig. 4.1).

We swept through two parameters, ϵ and Ω , in order to study the transitions between these behaviours (Fig. 4.3A). We note that the oscillatory behaviours of the ODE system is dependent on the fast-slow dynamics established by small values of ϵ . We conjecture that the second transition into the oscillating regime, along decreasing values of Ω and for small values of ϵ , occurs in conjunction with a canard explosion, (noted with a star on Fig. 4.3A).

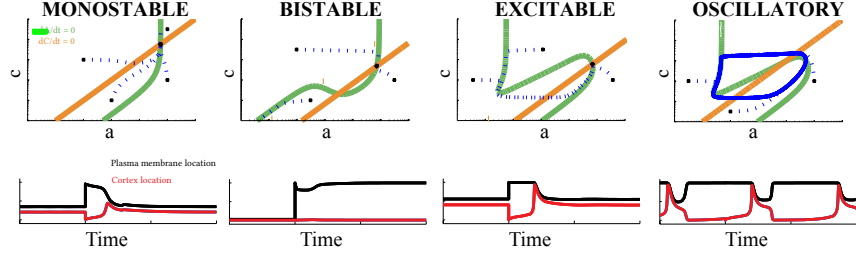


Figure 4.1: Four possible behaviour regimes of the ODE system (Equations 3.16, 3.17).

A canard explosion is a false bifurcation arising near a hopf bifurcation and is characterized by a jump from a single steady state solution to large amplitude oscillations with a small change in the parameter, such as in Fig. 4.2. This is a known feature exhibited by some fast-slow dynamical systems [50].

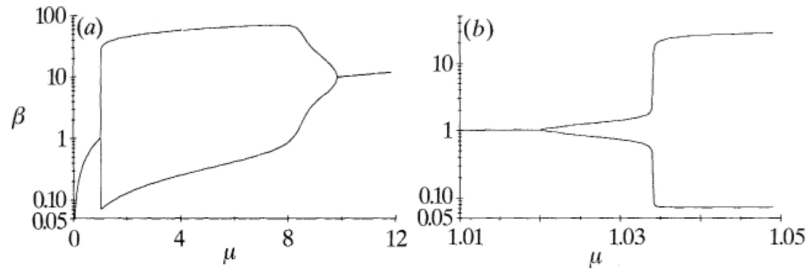


Figure 4.2: Canard in the autocatalator system described in [50].

We plan to demonstrate that our transition to oscillations is in fact a canard explosion by performing a two parameter bifurcation analysis to characterize the bifurcation lines and find the so-called *canard* point at which the oscillations appear to jump. The resulting bifurcation diagram might look something like the Fig. 4.3B.

4.3 Non local Maxwell Condition

We are seeking an analog of the Maxwell condition for the bleb model, and similar non-local PDEs. We will make progress toward on this by studying the following systems, from most general (Equations 4.1, 4.2) to most the most narrow (Equations 4.8, 4.7). In the fast timescale, we have $c = c^{ss}$. The dynamics of excitation are thus only governed by the a equation (Equation 3.11). We are ultimately interested in a necessary and sufficient traveling wave condition for the general system

$$\frac{\partial a}{\partial t} = f(a, y) \quad (4.1)$$

$$0 = g \left(a, y, \frac{\partial^2 y}{\partial x^2} \right). \quad (4.2)$$

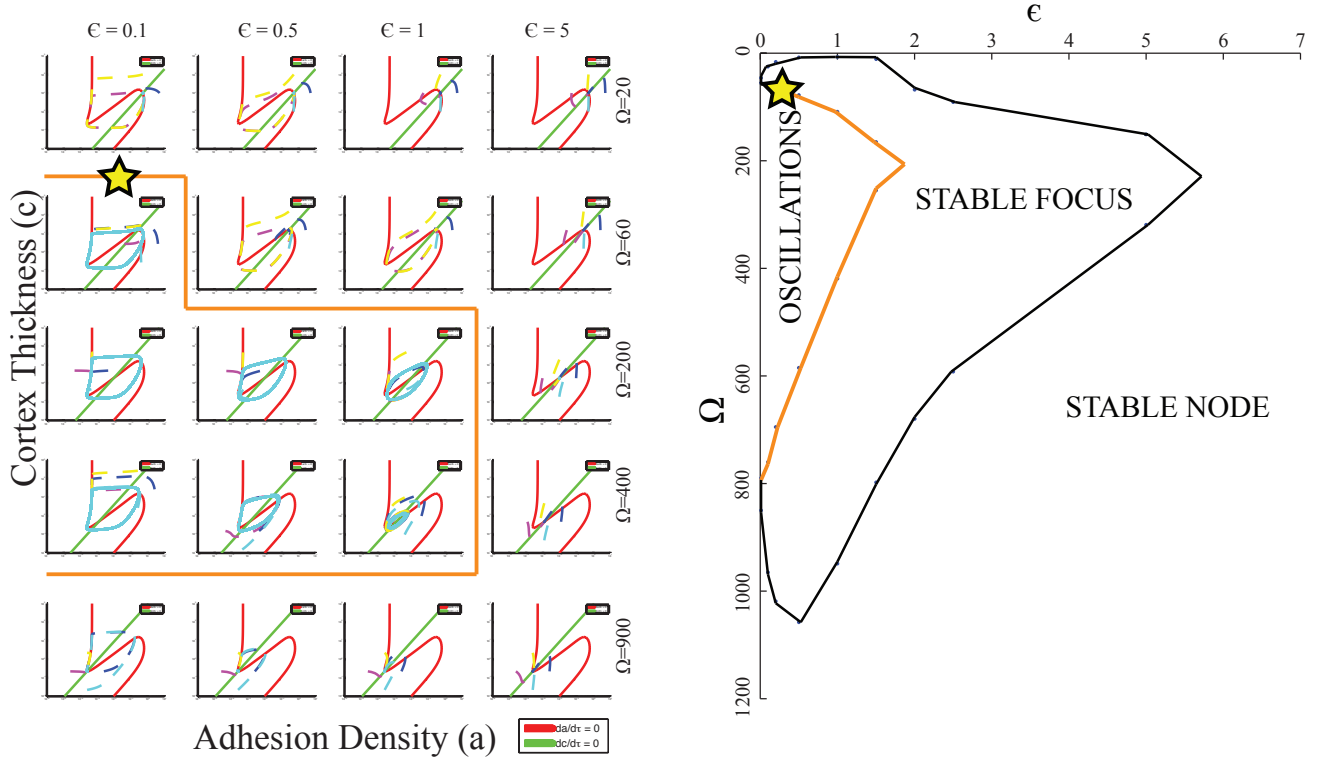


Figure 4.3: Left: Two parameter sweep noting changes in qualitative behaviour of the system. The star denotes the location of our hypothesized canard explosion. Right: Hypothetical two parameter bifurcation diagram.

Our specific system restricted to the fast timescale is

$$\frac{\partial a}{\partial t} = \frac{c^{ss}}{1 + c^{ss}} \exp\left(-\frac{y - y_C}{D}\right) - a \exp\left(\frac{y - y_C}{F}\right) \quad (4.3)$$

$$0 = -a(y - y_C) + P(1 - y) + \gamma_M \frac{\partial^2 y}{\partial x^2} \quad (4.4)$$

$$0 = a(y - y_C) - Mcy_C. \quad (4.5)$$

Note that since Eq. 4.5 is algebraic in y_C , we can eliminate it from the system. A narrow version of the system is obtained if we assume the force balance equations are linear in a .

$$\frac{da}{dt} = f_1(y) - af_2(y) \quad (4.6)$$

$$0 = g_1(y) - ag_2(y) + \frac{\partial^2 y}{\partial x^2} \quad (4.7)$$

This can be obtained from our system given the following simplifying assumption. Assume that the variable, y_C , does not move significantly during excitation, $y_C = y_C^{ss}$, leaving us

with a new system of two equations:

$$\frac{\partial a}{\partial t} = \frac{c^{ss}}{1 + c^{ss}} \exp\left(-\frac{y - y_C^{ss}}{D}\right) - a \exp\left(\frac{y - y_C^{ss}}{F}\right) \quad (4.8)$$

$$0 = -a(y - y_C^{ss}) + P(1 - y) + \gamma_M \frac{\partial^2 y}{\partial x^2} \quad (4.9)$$

We derive a necessary condition for the system described by Equations 4.8 and 4.7 here.

Numerically, we observe a travelling wave solution to the reduced system described by equations 4.8, and 4.9 and is shown in Fig. 4.4.

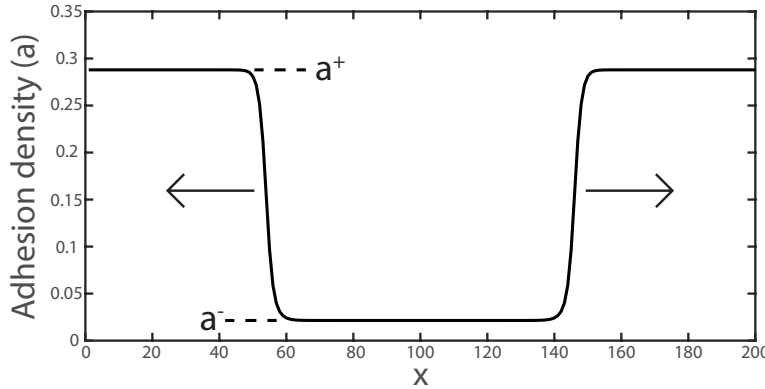


Figure 4.4: Snapshot of the travelling wave from simulation of Eq. 4.8 and 4.9.

4.3.1 Transformation to z coordinate and derivation of non-local Maxwell condition

We assume, WLOG, that Eq. 4.6 has two stable roots which we will denote by (y^+, a^+) and (y^-, a^-) . Transform to wave coordinate $z = x - vt$ and 4.6 and 4.7 become:

$$-v \frac{da}{dz} = f_1(y) - af_2(y) \quad (4.10)$$

$$0 = g_1(y) - ag_2(y) + \frac{\partial^2 y}{\partial z^2} \quad (4.11)$$

We can use Eq. 4.11 to solve for a :

$$a = \frac{1}{g_2(y)} \left(g_1(y) + \frac{\partial^2 y}{\partial z^2} \right) \quad (4.12)$$

Then it follows that:

$$\Rightarrow -v \frac{\partial a}{\partial z} = f_1(y) - \frac{g_1(y)}{g_2(y)} f_2(y) - \frac{f_2(y)}{g_2(y)} \frac{\partial^2 y}{\partial z^2} \quad (4.13)$$

Multiply by $\frac{g_2(y)}{f_2(y)}$,

$$\Rightarrow -v \frac{\partial a}{\partial z} \frac{g_2(y)}{f_2(y)} = f_1(y) \frac{g_2(y)}{f_2(y)} - g_1(y) - \frac{\partial^2 y}{\partial z^2} \quad (4.14)$$

Multiply by $\frac{\partial y}{\partial z}$,

$$\Rightarrow -v \frac{\partial a}{\partial z} \frac{g_2(y)}{f_2(y)} \frac{\partial y}{\partial z} = \left(f_1(y) \frac{g_2(y)}{f_2(y)} - g_1(y) - \frac{\partial^2 y}{\partial z^2} \right) \frac{\partial y}{\partial z} \quad (4.15)$$

Integrate over z ,

$$\Rightarrow \int_{-\infty}^{\infty} -v \frac{\partial a}{\partial z} \frac{g_2(y)}{f_2(y)} \frac{\partial y}{\partial z} dz = \int_{-\infty}^{\infty} \left(f_1(y) \frac{g_2(y)}{f_2(y)} - g_1(y) - \frac{\partial^2 y}{\partial z^2} \right) \frac{\partial y}{\partial z} dz \quad (4.16)$$

Change variables on RHS,

$$\Rightarrow -v \int_{-\infty}^{\infty} \frac{\partial a}{\partial z} \frac{g_2(y)}{f_2(y)} \frac{\partial y}{\partial z} dz = \int_{y^-}^{y^+} \left(f_1(y) \frac{g_2(y)}{f_2(y)} - g_1(y) - \frac{\partial^2 y}{\partial z^2} \right) dy \quad (4.17)$$

$$\Rightarrow -v \int_{-\infty}^{\infty} \frac{\partial a}{\partial z} \frac{g_2(y)}{f_2(y)} \frac{\partial y}{\partial z} dz = \int_{y^-}^{y^+} \left(f_1(y) \frac{g_2(y)}{f_2(y)} - g_1(y) \right) dy - \int_{y^-}^{y^+} \frac{\partial^2 y}{\partial z^2} dy \quad (4.18)$$

$$\Rightarrow -v \int_{-\infty}^{\infty} \frac{\partial a}{\partial z} \frac{g_2(y)}{f_2(y)} \frac{\partial y}{\partial z} dz = \int_{y^-}^{y^+} \left(f_1(y) \frac{g_2(y)}{f_2(y)} - g_1(y) \right) dy \quad (4.19)$$

The Non-local Maxwell Condition Number is defined by the RHS of the above equation. In our specific case,

$$f_1(y) = \frac{c^{ss}}{1 + c^{ss}} \exp \left(-\frac{y - y_C^{ss}}{D} \right), \quad (4.20)$$

$$f_2(y) = \exp \left(\frac{y - y_C^{ss}}{F} \right), \quad (4.21)$$

$$g_1(y) = P(1 - y), \quad (4.22)$$

$$g_2(y) = (y - y_C^{ss}). \quad (4.23)$$

Therefore,

$$\begin{aligned}
& -v \int_{-\infty}^{\infty} \frac{\partial a}{\partial z} \frac{(y - y_C^{ss})}{\exp\left(\frac{y - y_C^{ss}}{F}\right)} \frac{\partial y}{\partial z} dz \\
&= \int_{y^-}^{y^+} \left(\frac{c^{ss}}{1 + c^{ss}} \exp\left(-\frac{y - y_C^{ss}}{D}\right) \frac{(y - y_C^{ss})}{\exp\left(\frac{y - y_C^{ss}}{F}\right)} - P(1 - y) \right) dy \quad (4.24)
\end{aligned}$$

$$\begin{aligned}
\implies & -v \int_{-\infty}^{\infty} \frac{\partial a}{\partial z} \frac{\partial y}{\partial z} \exp\left(-\frac{y - y_C^{ss}}{F}\right) (y - y_C^{ss}) dz \\
&= \int_{y^-}^{y^+} \left(\frac{c^{ss}}{1 + c^{ss}} \exp\left(-\left(\frac{1}{D} + \frac{1}{F}\right)(y - y_C^{ss})\right) - P(1 - y) \right) dy \quad (4.25)
\end{aligned}$$

We also note that in our specific case $y^- > y^+$ and so it makes sense to integrate from y^+ to y^- .

$$\begin{aligned}
&\Rightarrow -v \int_{-\infty}^{\infty} \frac{\partial a}{\partial z} \frac{\partial y}{\partial z} \exp\left(-\frac{y - y_C^{ss}}{F}\right) (y - y_C^{ss}) dz \\
&= - \int_{y^+}^{y^-} \left(\frac{c^{ss}}{1 + c^{ss}} \exp\left(-\left(\frac{1}{D} + \frac{1}{F}\right)(y - y_C^{ss})\right) - P(1 - y) \right) dy
\end{aligned}$$

Our Non-Local Maxwell condition Number is:

$$NLMC = - \int_{y^+}^{y^-} \left(\frac{c^{ss}}{1 + c^{ss}} \exp\left(-\left(\frac{1}{D} + \frac{1}{F}\right)(y - y_C^{ss})\right) - P(1 - y) \right) dy \quad (4.26)$$

$$\begin{aligned}
&= \frac{c^{ss}}{1 + c^{ss}} \exp\left(+\left(\frac{1}{D} + \frac{1}{F}\right)y_C^{ss}\right) (y^- - y^+) + P \left(1 - \frac{1}{2} \left((y^+)^2 - (y^-)^2\right)\right) \\
&\quad (4.27)
\end{aligned}$$

The integral on the LHS is of determined sign (-). Therefore, the Nonlocal Maxwell Condition is:

$NLMC > 0 \Rightarrow v$ exists, travelling solution

$NLMC < 0 \Rightarrow v$ does not exist, stationary solution

Note that only the second line (necessity) is shown here. The first line (sufficiency) is supported by numerical evidence below.

4.3.2 Numerical Results

After we hold c and y_C constant, we end up with a single PDE. Dropping the spatial term, and analyzing the single ODE we find that the ODE is can be monostable low, monostable high, in which case there is a single steady state solution or it can be bistable. See Fig. 4.5 for a plot of the single ODE in the various regimes.

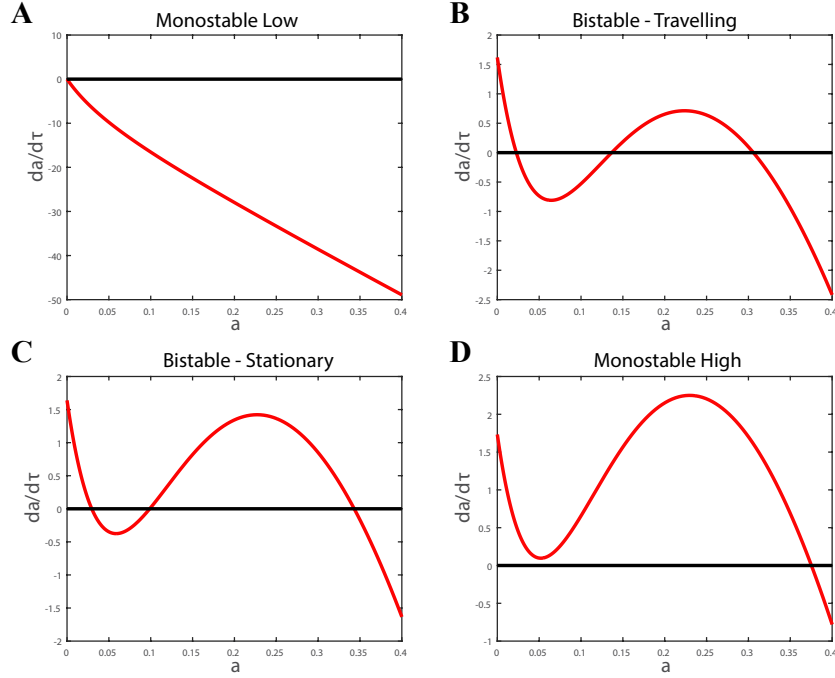


Figure 4.5: Plot of da/dt vs a for four different parameter sets. A) The monostable low case, $\Omega = 57$ and $F = 0.95$. B) The bistable ODE-travelling PDE regime, $\Omega = 55$ and $F = 1.2$. C) The bistable ODE-stationary PDE regime, $\Omega = 50$ and $F = 1.4$. D) The monostable high case, $\Omega = 45$ and $F = 1.55$.

The non-local Maxwell condition is equal to 0 in both of the monostable regimes (because $y^- = y^+$), but can be negative or positive in the bistable regime. Returning to the PDE, we don't expect travelling solutions to arise from a monostable regime, but we wish to see for which region of the bistable regime the non-local Maxwell condition predicts travelling solutions. By varying two parameters continuously we can determine these regions. This is shown in Fig. 4.6(A). Here the parameters varied are Ω which is not present in the single PDE but changes are reflected in c^{ss} , and F . We plan to create identical plots using other pairs of parameters. The regions shown in Fig. 4.6 (A) match up well with the numerical solutions of the PDE as depicted in Eq. 4.6 (B), which shows the velocity of the travelling wave solution ($= 0$ for a stationary solution).

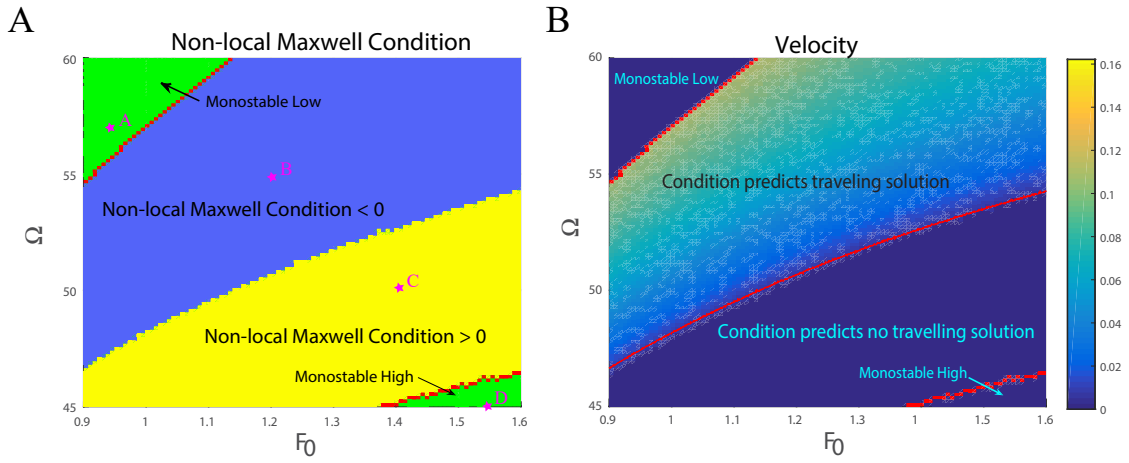


Figure 4.6: (A) The results of varying two parameters Ω and F and the regions where the non-local Maxwell condition is either greater than 0 (yellow) or less than 0 (blue). Red lines indicate the boundaries between the monostable and bistable regimes. The pink stars correspond to locations in parameter space where the corresponding phaseline plots of Fig. 4.5 were made. (B) Velocity resulting from numerical solutions of the PDE as two parameters are varied. Red lines indicate the boundaries between the monostable and bistable regimes, as well as the line across which the non-local Maxwell condition is equal to 0.

5. Nuclear blebs

5.1 Introduction

Cardiomyopathies and arrhythmia are conditions with high morbidity and limited therapies. Although a vast number of genes have been discovered to contribute to the etiology of these diseases, translational research, the practical application of genetic knowledge to improve screening, diagnosis, and treatment for affected individuals and their families has been limited. One major obstacle is the lack of understanding of the relationship between genotype and emergent phenotype, the mechanisms by which pathologies occur, and the identification of factors that cause clinical variability between and within families. Our collaborators in the Grosberg and Zargoza labs are currently studying three affected families each with different mutation in the Lamin A/C (LMNA) gene. LMNA, together with LMNB1 and LMNB2, encode the main proteins of the nuclear lamina, the structural matrix of the nuclear envelope that interacts with both chromatin in the cell nucleus and the cytoskeleton [9]. In their experiments, it has been observed that the nuclei often have a wide variety of geometrical defects, including rounded protrusions which we will refer to as nuclear blebs, as in Fig. 5.1. This is a known property of LMNA mutated cell lines (such as in progeria), however the mechanisms by which such defects form are unclear. It is known that the LMNA mutation impacts the nuclear lamina, which is present at the inner layer of the nuclear membrane. As a key component of the nuclear lamina, lamin plays an important role in nucleus-cytoplasm interaction and signaling through lamin-binding protein complexes including SUN and KASH that span the nuclear membrane [30]. Cells in this line of experiments come from patients with heart disease (i.e., cardiomyopathy and/or arrhythmias), and they exhibit a mutation in a gene that is known to correlate with nuclear defects. In addition, our collaborators have control cells from people without heart diseases from the same family as the patients' cells. Nuclei from both patient and control cell lines have been imaged, and a variety of nuclear shapes in the two types of cells has been found. Nuclear blebbing involves dynamic, complex interactions among many elements: The nuclear lamina, nuclear membrane, membrane-lamin linkers, and chromatin. Preliminary studies have found that both control (fibroblasts of human origin with no mutation) and patient (fibroblasts from patients with the mutation) exhibit some number of defects. We hypothesize a correlation between nuclear shape types and cardiomyopathies and arrhythmias. Therefore we have an ideal system in which to investigate a possible correlation between specific nuclear defects and disease states.

We will use mathematical modelling to test the hypothesis that abnormal nuclear shapes in patients arise due to a mechanical anomaly in the lamin protein due to the mutation in

LMNA. this will allow us to differentiate between the type of defects expected under normal biological variability vs. in a pathological situation.

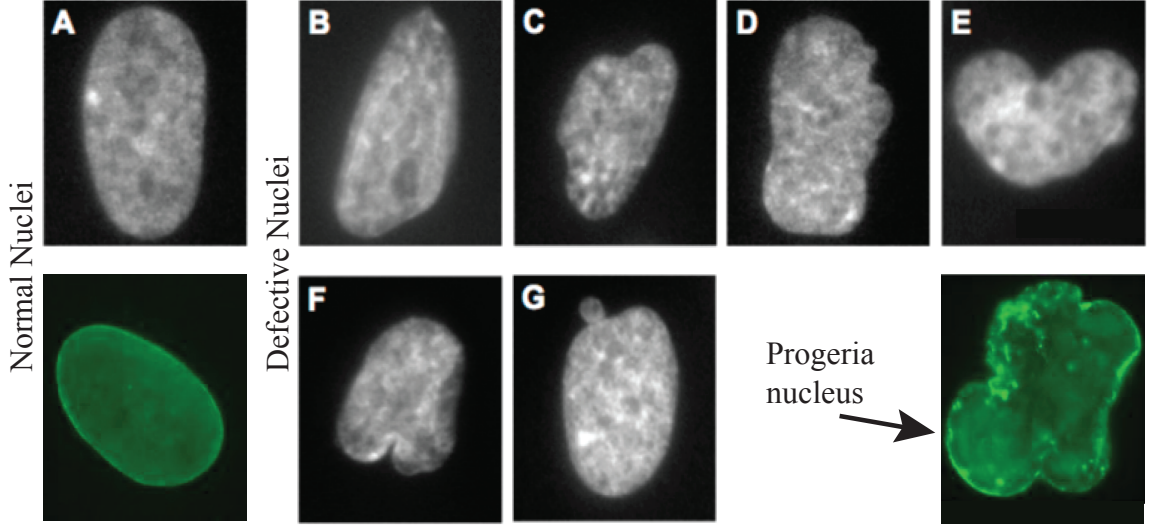


Figure 5.1: Defective nuclei have an irregular shape as compared to normal nuclei. In particular, there may exist one or more protusions at the boundary resulting in a concave nuclei.

5.2 Model

5.2.1 Statement of the model

We developed a model which consists of 2 dynamic variables representing the line density of lamin A/C, $a(t)$, and lamin B, $b(t)$, as functions of time, t on a simple closed curve in 2D, $s(t)$, enclosing an area, $\mathcal{A}(t)$. The details of laminA/C (B) assembly and disassembly into the lamina are unknown, we assume usual assembly kinetics and allow for possible feedback in the disassembly terms. It is known that lamin proteins are not confined to the nuclear lamina, but exist in the nucleoplasm where they may be performing other functions, including gene regulation [32, 34]. We will assume there is a pool of nuclear lamins which exchanges dynamically with the the lamins in the nuclear lamina. The resulting equations are:

$$\frac{\partial a}{\partial t} = \frac{k_{on}^a}{\mathcal{A}(t)} a_{nuc} - k_{off}^a(s, b) a \quad (5.1)$$

$$\frac{\partial b}{\partial t} = \frac{k_{on}^b}{\mathcal{A}(t)} b_{nuc} - k_{off}^b(s, a) b \quad (5.2)$$

The parameters k_{on}^a, k_{on}^b govern assembly of lamin A/C, and lamin B into the lamina, respectfully. The functions $k_{off}^a(s, b) = k_{off}^{0a} + \Phi_a(s, b)$ and $k_{off}^b(s, a) = k_{off}^{0b} + \Phi_b(s, a)$ describe

laminar turnover with possible feedback terms arising from Φ to be explored in future work and will be further discussed in Section 5.3. The nuclear pools of lamin A/C (B) are labelled by $a_{nuc}(b_{nuc})$. We therefore have the following conservation of lamin equations:

$$a_{tot} = \int_0^{\mathcal{L}_0} a(s, t) ds + a_{nuc} \quad (5.3)$$

$$b_{tot} = \int_0^{\mathcal{L}_0} b(s, t) ds + b_{nuc} \quad (5.4)$$

Where \mathcal{L}_0 is the length of the perimeter of a nucleus. These equations are coupled to a mechanical description of the lamina via the energy functional:

$$\mathcal{E} = \mathcal{E}_{stretch} + \mathcal{E}_{pressure} + \mathcal{E}_{bending} + \mathcal{E}_{cytoskeleton} + k_B T \xi \quad (5.5)$$

Where

$$\mathcal{E}_{stretch} = \int_0^{\mathcal{L}_0} \frac{1}{2} (\mathcal{G}_a(a(s)) + \mathcal{G}_b(b(s))) \left(\left\| \frac{\partial \vec{x}}{\partial s} \right\| - 1 \right)^2 ds \quad (5.6)$$

$$\mathcal{E}_{pressure} = \mathcal{P} \left(\frac{A}{A_0} - 1 \right)^2 \quad (5.7)$$

$$\mathcal{E}_{bending} = \int_0^{\mathcal{L}_0} \frac{1}{2} (\mathcal{M}_a(a(s)) + \mathcal{M}_b(b(s))) \left\| \frac{\partial^2 \vec{x}}{\partial s^2} \right\|^2 ds \quad (5.8)$$

$$\mathcal{E}_{cytoskeleton} = \int_0^{\mathcal{L}_0} \mathcal{F}_{cyto}(a(s)) \Theta(\theta) ||\vec{x}|| ds \quad (5.9)$$

and

$$\Theta(\theta) = \frac{e^{\cos(2\theta)/\sigma_{VM}}}{\int_0^{2\pi} e^{\cos(2\theta)/\sigma_{VM}} d\theta}$$

The lamina is modeled as an elastic material where the first term, $\mathcal{E}_{stretch}$ corresponds to laminar surface tension. The next term, $\mathcal{E}_{pressure}$ is the intranuclear pressure, possibly due to chromatin. The third term, $\mathcal{E}_{bending}$ is bending resistance terms due to lamin-lamin crosslinking. It is known that there are non-negligible forces produced by the cellular cytoskeleton (actin and microtubules) which act on the lamins via nuclear transmembrane proteins [28] and so the fourth term, $\mathcal{E}_{cytoskeleton}$, is due to this. Finally we include a term for thermal fluctuations generalized to 2D, $k_B T \xi$. A cartoon schematic of the model is shown in Fig. 5.2.

Several of the mechanical parameters are in fact functions of the local densities of laminar lamin proteins, thus connecting the mechanical properties of the lamina (and therefore the nucleus) to the mechanical properties of lamin. A complete list of parameter descriptions can be found in Table 5.1.

We non dimensionalized the system by choosing characteristic scales for length, time,

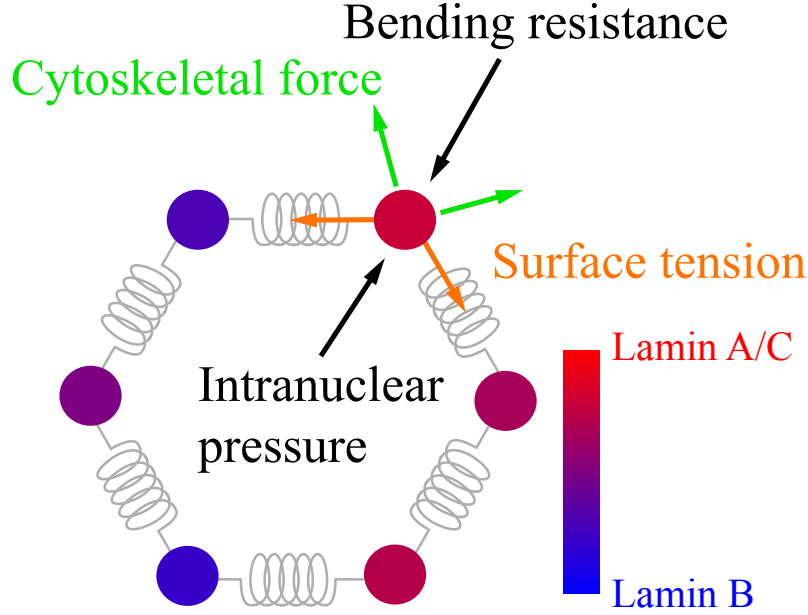


Figure 5.2: Schematic diagram of the model including Lamin A/C/B densities, and the forces acting on the lamina.

Table 5.1: Mechanical parameters.

Symbol	Dimensions	Meaning
\mathcal{G}_a	[pN]	Stretch modulus associated with lamin A/C
\mathcal{G}_b	[pN]	Stretch modulus associated with lamin B
\mathcal{P}	[pN μm]	Bulk modulus
\mathcal{L}_0	[μm]	Resting perimeter of nucleus
\mathcal{M}_a	[pN μm^2]	Bending modulus associated with lamin A/C
\mathcal{M}_b	[pN μm^2]	Bending modulus associated with lamin B
θ	[rad]	Angle
\mathcal{F}_{cyto}	[pN / μm]	Force line density of the cytoskeleton
σ_{VM}	[dimensionless]	Concentration of distribution of cytoskeletal force

energy and amount of lamin. The details of this non-dimensionalization procedure can be found in Appendix A.2. The resulting non-dimensional system is expressed by the following system of equations:

$$\frac{\partial A}{\partial \tau} = \kappa_{on} \frac{1}{\lambda(\tau)} A_{nuc} - (\kappa_{off} + \phi_A(S, B))A, \quad (5.10)$$

$$\frac{\partial B}{\partial \tau} = \frac{1}{\lambda(\tau)} B_{nuc} - (1 + \phi_B(S, A))B \quad (5.11)$$

$$(5.12)$$

Table 5.2: Non-dimensionalized variable.

Symbol	Meaning
A	Laminar non-dimensionalized density of Lamin A/C
B	Laminar non-dimensionalized density of Lamin B
A_{nuc}	Nucleoplasmic lamin A/C
B_{nuc}	Nucleoplasmic lamin B
S	Non-dimesionalized position of the lamina
$\lambda(\tau)$	Non-dimesionalized area of nucleus

Table 5.3: Non-dimensionalized (ND) parameters.

Symbol	Meaning
κ_{on}	ND rate constant associated with lamin A/C incorporation into the lamina
κ_{off}	ND rate constant associated with lamin A/C dissociation from the lamina
G_A	ND stretch modulus associated with lamin A/C
G_B	ND stretch modulus associated with lamin B
Π	ND bulk modulus
λ_0	Resting non-dimensionalized area of nucleus
M_A	ND bending modulus associated with lamin A/C
M_B	ND bending modulus associated with lamin B
θ	Angle
F_{cyto}	ND force line density of the cytoskeleton

With Energy

$$E = \int_0^{2\sqrt{\pi}} \frac{1}{2} (G_A(A(S)) + G_B(B(S))) \left(\left\| \frac{\partial \vec{\chi}}{\partial S} \right\| - 1 \right)^2 dS + \Pi \left(\frac{\lambda(\tau)}{\lambda_0} - 1 \right)^2 \quad (5.13)$$

$$+ \int_0^{2\sqrt{\pi}} \frac{1}{2} (M_A(A(S)) + M_B(B(S))) \left\| \frac{\partial^2 \vec{\chi}}{\partial S^2} \right\|^2 dS \quad (5.14)$$

$$+ \int_0^{2\sqrt{\pi}} F_{cyto}(A(S)) \Theta(\theta) \| \vec{\chi} \| dS + k_B T \xi \quad (5.15)$$

A description of non dimensional variables can be found in Table 5.2 and parameters in Table 5.3.

5.2.2 Numerical implementation of the model

The model is implemented in Matlab by discretizing the 2D simple closed curve into a series of nodes connected by linear springs with an elastic modulus dependent on the amount of lamins at the two nodes on either side of each spring. We solve the ODE systems using the forward Euler method. The energy minimization is done using a Markov chain Monte Carlo method at each step forward in time.

5.2.3 Tuning the model

Many of the mechanical parameters of the model are unknown because they are difficult or impossible to measure experimentally. We therefore have to tune the parameters in our model using some data. We used data from a series of experiments conducted on rat cardiomyocytes grown on fibronectin islands of various shapes and sizes as shown in Fig. 5.3 [20]. The features we extracted from the images are cellular aspect ratio, F-actin OOP (a measure of the anisotropy in the F-actin network), nuclear eccentricity, nuclear area, and nuclear perimeter.

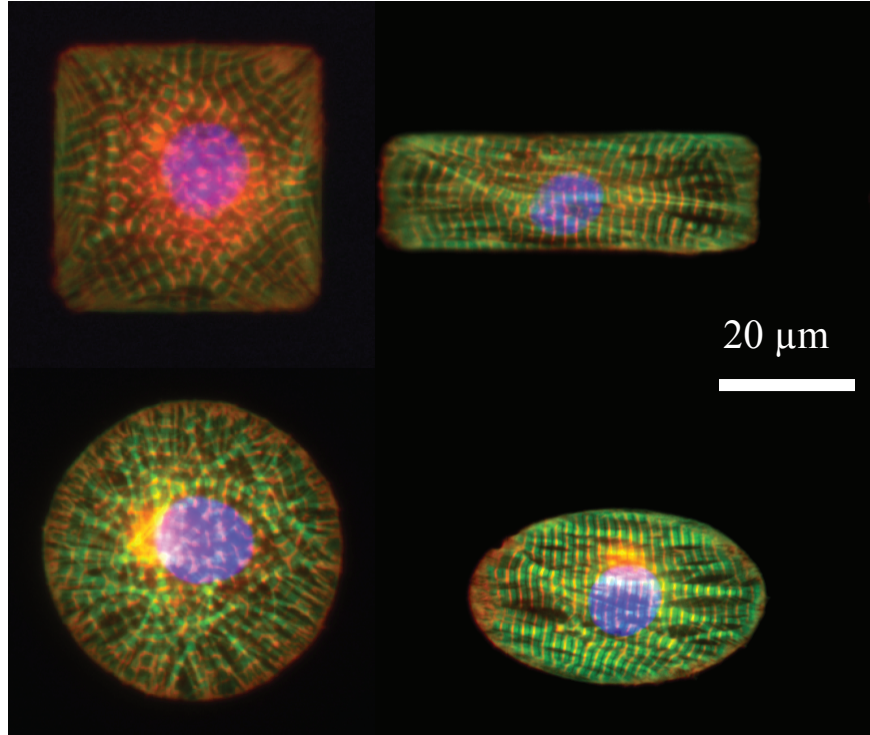


Figure 5.3: Rat cardiomyocytes grown on fibronectin islands of various shapes and sizes. [20].

In order to extract information about the correlations between these features we plotted each against the others in a scatter plot matrix, see Fig. 5.4. While most of the data appear uncorrelated, there is a clear correlation between F-actin OOP and nuclear eccentricity ($R^2 = 0.42$), and other attributes suitable for fitting. In particular, we chose three patterns in the data to fit our model, nuclear area, nuclear perimeter and correlation between F-actin OOP and nuclear eccentricity. We first chose a subset of the cell which have low F-actin OOP and tuned parameters to match the histograms of nuclear area and nuclear perimeter in both mean and standard deviation. This subset of cells was chosen so that we could assume isotropic cytoskeletal force and therefore set it to 0. Once these parameters were tuned (Fig. 5.5), we returned to the entire data set and tuned our model to match the eccentricity vs F-actin OOP plot, see Fig. 5.6. This gave us estimate of F_{cyto} which is in fact a ratio of two dimensional quantities, \mathcal{F}_{cyto} and \mathcal{G}_b . Since the traction force of actin has been measured experimentally [38], we were able to back-calculate and to obtain order of

Table 5.4: Order of magnitude parameter estimations.

Parameter	Estimate
$\mathcal{G}_a, \mathcal{G}_b$	$10^0 - 10^1$ pN
\mathcal{P}	$10^0 - 10^1$ pN·μm
\mathcal{L}_0	28 μm fds
$\mathcal{M}_a, \mathcal{M}_b$	$10^4 - 10^5$ pN·μm ²]
\mathcal{F}_{cyto}	$10^3 - 10^4$ pN/μm

magnitude estimates for all our mechanical parameters. These estimates are summarized in Table 5.4.

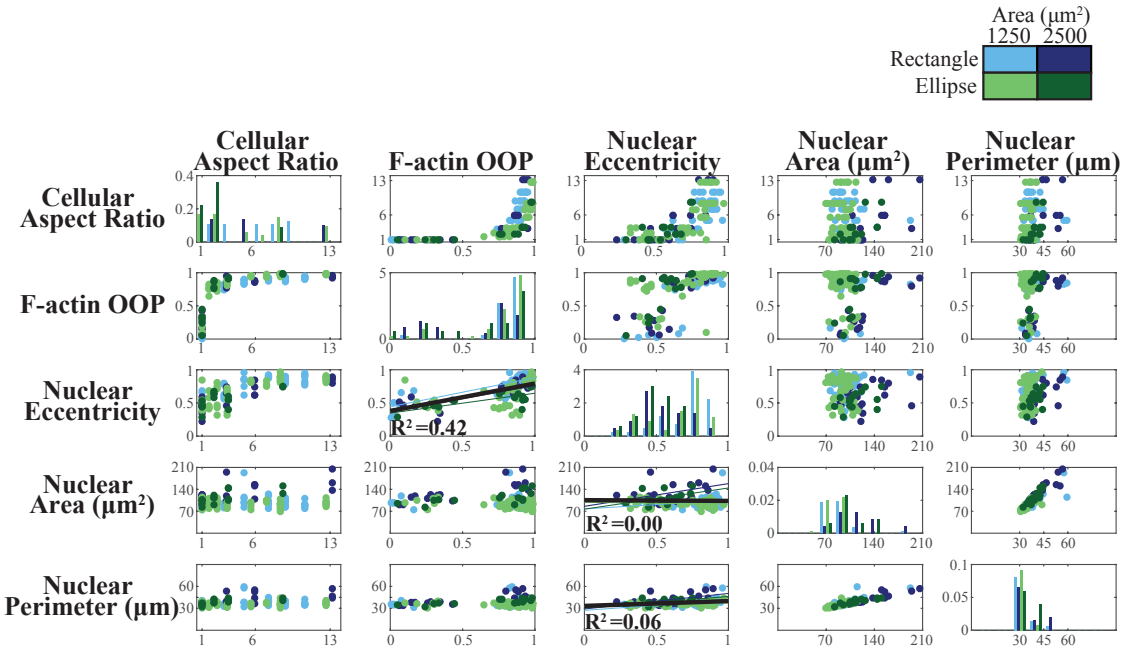


Figure 5.4: Matrix of scatter plots between features of the experimental data. Note that along the diagonal, the distributions of each feature are plotted.

5.3 Future work

The goal of this work is to reliably reproduce nuclear shape deformations. This requires a symmetry break in the system governing laminar assembly/disassembly dynamics. We plan to achieve this by including a feedback term in the functions $k_{off}^{a,b}$. Hypothesized sources of feedback include competition between lamin types, and stress induced feedback. These ideas are shown schematically in Fig. 5.7. Once we have established a symmetry break, we will explore perturbations to the model which correspond to physical changes in the lamin A/C protein which can best reproduce patient versus control data. These potential perturbations are summarized in Table 5.5

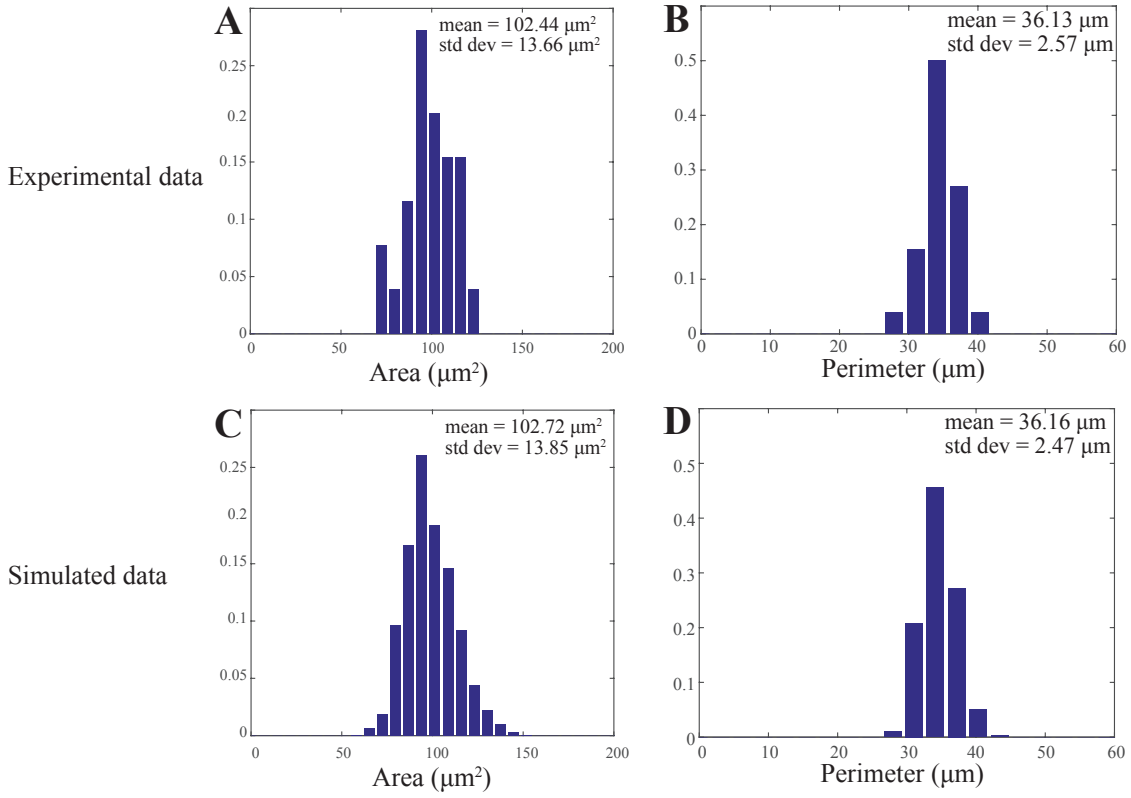


Figure 5.5: Histogram matching model to experimental data. Experimental histograms of nuclear area (A) and nuclear perimeter (B) of cell with aspect ratio 1. Simulated histograms of nuclear area (C) and nuclear perimeter (D) of simulated nuclei with no active cytoskeletal force.

Table 5.5: Potential perturbations.

Model perturbation	Change in lamin A/C
Decrease total amount of lamin A/C	Haploinsufficiency
Modify assembly/disassembly rates	Abnormal localization of lamin
Modify \mathcal{G}_a (elastic modulus)	Weaken molecular strength of Lamin A/C
Modify \mathcal{M}_a (bending modulus)	Weaken Lamin A/C-Lamin A/C crosslinking
Modify $\mathcal{F}_{cyto}, \sigma_{VM}$	Weaken transmembrane link
Modify feedback from lamin B	Modify interaction with Lamin B

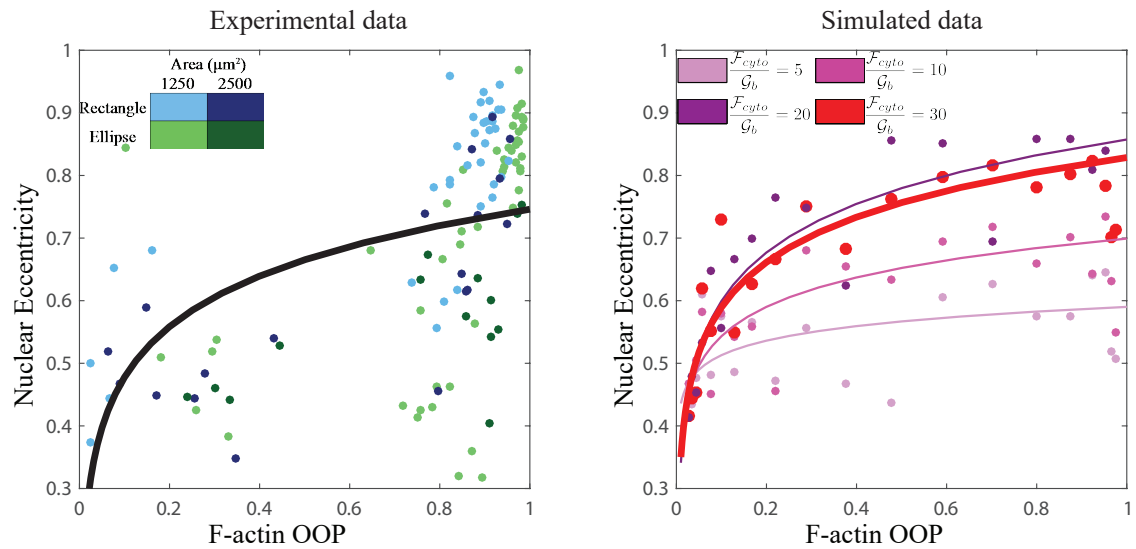


Figure 5.6: \mathcal{F}_{cyto} was obtained by matching the correlation between F-actin OOP and nuclear eccentricity observed experimentally.

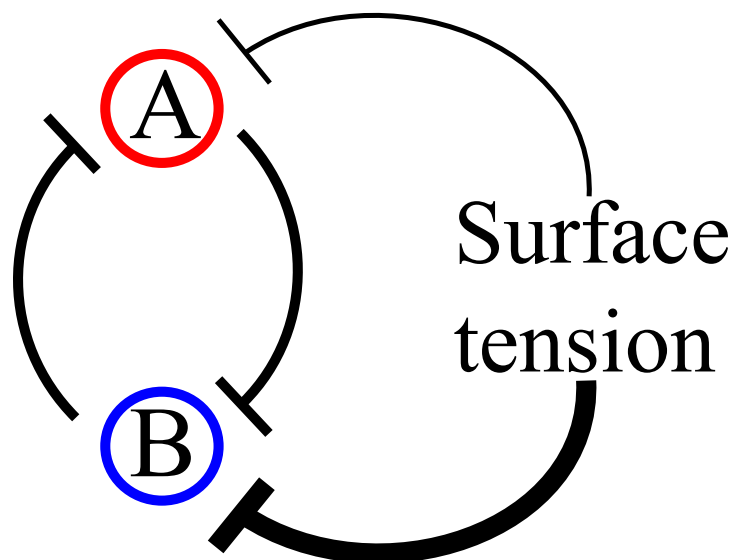


Figure 5.7: Schematic diagram of the possible sources of feedback in the model.

6. Timeline of Completion

Spring 2017 Advancement Completion of coursework	Summer 2017 Project 2: Two parameter bifurcation diagram Characterise canard explosion Project 3: Explore different feedback models to break symmetry
Fall 2017 Project 2: Literature review on integro-PDES in biology Demonstrate numerical sufficiency of NLMC for different parameter sweep Project 3: Detailed comparison of modelled nuclear defects to patient/control nuclear defects to determine hypothesized mechanism of defect	Winter 2018 Project 2: Submit manuscript to journal Project 3: Generate testable hypotheses based on nuclear bleb modelling results
Spring 2018 Project 3: Submit manuscript PhD Defense	Summer 2018

Figure 6.1: Timeline of completion.

Bibliography

- [1] R. Alert, J. Casademunt, J. Brugués, and P. Sens. Model for Probing Membrane-Cortex Adhesion by Micropipette Aspiration and Fluctuation Spectroscopy. *Biophysj*, 108(8):1878–1886, apr 2015.
- [2] J. Allard and A. Mogilner. Traveling waves in actin dynamics and cell motility. *Current Opinion In Cell Biology*, 25(1):1–9, sep 2012.
- [3] J. F. Allard, O. Dushek, D. Coombs, and P. A. Van Der Merwe. Mechanical Modulation of Receptor-Ligand Interactions at Cell-Cell Interfaces. *Biophysical Journal*, 102(6):1265–1273, mar 2012.
- [4] D. A. Baum and B. Baum. An inside-out origin for the eukaryotic cell. *BMC biology*, 12(1):76, 2014.
- [5] W. M. Bement, M. Leda, A. M. Moe, A. M. Kita, M. E. Larson, A. E. Golding, C. Pfeuti, K.-C. Su, A. L. Miller, A. B. Goryachev, and Others. Activator-inhibitor coupling between Rho signalling and actin assembly makes the cell cortex an excitable medium. *Nature Cell Biology*, 2015.
- [6] M. Biro, Y. Romeo, S. Kroschwitzl, M. Bovellan, A. Boden, J. Tcherkezian, P. P. Roux, G. Charras, and E. K. Paluch. Cell cortex composition and homeostasis resolved by integrating proteomics and quantitative imaging. *Cytoskeleton (Hoboken, N.J.)*, 70(11):741–754, nov 2013.
- [7] M. Bovellan, Y. Romeo, M. Biro, A. Boden, P. Chugh, A. Yonis, M. Vaghela, M. Fritzsche, D. Moulding, R. Thorogate, A. Jégou, A. J. Thrasher, G. Romet-Lemonne, P. P. Roux, E. K. Paluch, and G. Charras. Cellular Control of Cortical Actin Nucleation. *Current biology : CB*, 24(14):1628–1635, jul 2014.
- [8] N. F. Britton. Threshold phenomena and solitary traveling waves in a class of reaction-diffusion systems. *Siam Journal on Applied Mathematics*, 1982.
- [9] B. C. Capell and F. S. Collins. Human laminopathies: nuclei gone genetically awry. *Nature Reviews Genetics*, 7(12):940–952, 2006.
- [10] A. Carlson and L. Mahadevan. Elastohydrodynamics and kinetics of protein patterning in the immunological synapse. may 2015.

- [11] G. Charras and E. Paluch. Blebs lead the way: how to migrate without lamellipodia. *Nature Reviews Molecular Cell Biology*, 9(9):730–736, sep 2008.
- [12] G. T. Charras. A short history of blebbing. *Journal of microscopy*, 231(3):466–478, sep 2008.
- [13] G. T. Charras, M. Coughlin, T. J. Mitchison, and L. Mahadevan. Life and times of a cellular bleb. *Biophysical Journal*, 94(5):1836–1853, mar 2008.
- [14] G. T. Charras, T. J. Mitchison, and L. Mahadevan. Animal cell hydraulics. *Journal of Cell Science*, 122(Pt 18):3233–3241, sep 2009.
- [15] G. T. Charras, J. C. Yarrow, M. A. Horton, L. Mahadevan, and T. J. Mitchison. Non-equilibration of hydrostatic pressure in blebbing cells. *Nature*, 435(7040):365–369, may 2005.
- [16] A. G. Clark, K. Dierkes, and E. K. Paluch. Monitoring Actin Cortex Thickness in Live Cells. *Biophysj*, 105(3):570–580, aug 2013.
- [17] A. G. Clark, O. Wartlick, G. Salbreux, and E. K. Paluch. Stresses at the Cell Surface during Animal Cell Review Morphogenesis. *Current biology : CB*, 24(10):R484—R494, may 2014.
- [18] G. Danuser, J. Allard, and A. Mogilner. Mathematical Modeling of Eukaryotic Cell Migration: Insights Beyond Experiments. *Annual Review of Cell and Developmental Biology*, 29(1):130802122809007, nov 2012.
- [19] T. M. Dobrowsky, B. R. Daniels, R. F. Siliciano, S. X. Sun, and D. Wirtz. Organization of Cellular Receptors into a Nanoscale Junction during HIV-1 Adhesion. *PLoS Computational Biology*, 6(7):e1000855, jul 2010.
- [20] N. K. Drew, N. E. Johnsen, J. Q. Core, and A. Grosberg. Multiscale Characterization of Engineered Cardiac Tissue Architecture. *Journal of Biomechanical Engineering*, 138(11):111003, 2016.
- [21] L. Edelstein-Keshet. Mathematical models in biology. 1988.
- [22] R. FitzHugh. Impulses and Physiological States in Theoretical Models of Nerve Membrane. *Biophysical Journal*, 1(6):445–466, jul 1961.
- [23] B. Fogelson and A. Mogilner. Computational Estimates of Membrane Flow and Tension Gradient in Motile Cells. *PLoS ONE*, 9(1):e84524, jan 2014.
- [24] P. Friedl and K. Wolf. Tumour-cell invasion and migration: diversity and escape mechanisms. *Nature Reviews Cancer*, 3(5):362–374, may 2003.
- [25] M. Fritzsche, R. Thorogate, and G. Charras. Quantitative Analysis of Ezrin Turnover Dynamics in the Actin Cortex. *Biophysj*, 106(2):343–353, jan 2014.

- [26] N. Fujinami and T. Kageyama. Circus movement in dissociated embryonic cells of a teleost, *Oryzias latipes*. *Journal of Cell Science*, 19(1):169–182, oct 1975.
- [27] E. Hannezo, B. Dong, P. Recho, J.-F. Joanny, and S. Hayashi. Cortical instability drives periodic supracellular actin pattern formation in epithelial tubes. *Proceedings Of The National Academy Of Sciences Of The United States Of America*, 112(28):8620–8625, jul 2015.
- [28] F. Haque, D. Mazzeo, J. T. Patel, D. T. Smallwood, J. A. Ellis, C. M. Shanahan, and S. Shackleton. Mammalian SUN protein interaction networks at the inner nuclear membrane and their role in laminopathy disease processes. *Journal of Biological Chemistry*, 285(5):3487–3498, 2010.
- [29] W. Helfrich. *Elastic properties of lipid bilayers: theory and possible experiments*. Zeitschrift f{ü}r Naturforschung. Teil C: Biochemie, 1973.
- [30] C. Y. Ho and J. Lammerding. Lamins at a glance. *Journal of Cell Science*, 125(9):2087–2093, 2012.
- [31] A. R. Houk, A. Jilkine, C. O. Mejean, R. Boltyanskiy, E. R. Dufresne, S. B. Angenent, S. J. Altschuler, L. F. Wu, and O. D. Weiner. Membrane Tension Maintains Cell Polarity by Confining Signals to the Leading Edge during Neutrophil Migration. *Cell*, 148(1-2):175–188, jan 2012.
- [32] P. Hozák, A. M. Sasseville, Y. Raymond, and P. R. Cook. Lamin proteins form an internal nucleoskeleton as well as a peripheral lamina in human cells. *Journal of cell science*, 108 (Pt 2):635–644, 1995.
- [33] C.-H. Huang, M. Tang, C. Shi, P. A. Iglesias, and P. N. Devreotes. An excitable signal integrator couples to an idling cytoskeletal oscillator to drive cell migration. *Nature Cell Biology*, 15(11):1307–1316, oct 2013.
- [34] C. J. Hutchison. Lamins: building blocks or regulators of gene expression? *Nature Reviews Molecular Cell Biology*, 3(11):848–858, 2002.
- [35] T. Idema, T. Idema, J. O. Dubuis, J. O. Dubuis, L. Kang, L. Kang, M. L. Manning, M. L. Manning, P. C. Nelson, P. C. Nelson, T. C. Lubensky, and A. J. Liu. The syncytial Drosophila embryo as a mechanically excitable medium. *PLoS ONE*, 2013.
- [36] M. Kapustina, T. C. Elston, and K. Jacobson. Compression and dilation of the membrane-cortex layer generates rapid changes in cell shape. *Journal Of Cell Biology*, 200(1):95–108, jan 2013.
- [37] S. Kondo and T. Miura. Reaction-Diffusion Model as a Framework for Understanding Biological Pattern Formation. *Science*, 329(5999):1616 LP – 1620, sep 2010.
- [38] P. L. Kuo, H. Lee, M. A. Bray, N. A. Geisse, Y. T. Huang, W. J. Adams, S. P. Sheehy, and K. K. Parker. Myocyte shape regulates lateral registry of sarcomeres and contractility. *American Journal of Pathology*, 181(6):2030–2037, 2012.

- [39] J. Lee, A. Ishihara, J. A. Theriot, and K. Jacobson. Principles of locomotion for simple-shaped cells. *Nature*, 362(6416):167–171, 1993.
- [40] N. Leijnse, L. B. Oddershede, and P. M. Bendix. An updated look at actin dynamics in filopodia. *Cytoskeleton (Hoboken, N.J.)*, 72(2):71–79, feb 2015.
- [41] F. Y. Lim, K.-H. Chiam, and L. Mahadevan. The size, shape, and dynamics of cellular blebs. *Epl*, 100(2):28004, oct 2012.
- [42] J. Liu, Y. Sun, G. F. Oster, and D. G. Drubin. Mechanochemical crosstalk during endocytic vesicle formation. *Current Opinion In Cell Biology*, 22(1):36–43, feb 2010.
- [43] J. S. Logue, A. X. Cartagena-Rivera, M. A. Baird, M. W. Davidson, R. S. Chadwick, and C. M. Waterman. Erk regulation of actin capping and bundling by Eps8 promotes cortex tension and leader bleb-based migration. *eLife*, 4, jul 2015.
- [44] Y. Mori, A. Jilkine, and L. Edelstein-Keshet. Wave-pinning and cell polarity from a bistable reaction-diffusion system. *Biophysical Journal*, 94(9):3684–3697, may 2008.
- [45] J. D. Murray. *Mathematical Biology*. Springer Berlin Heidelberg, Berlin, Heidelberg, 1989.
- [46] E. C. Olson. Onset of electrical excitability during a period of circus plasma membrane movements in differentiating Xenopus neurons. *Journal of Neuroscience*, 16(16):5117–5129, aug 1996.
- [47] E. K. Paluch and E. Raz. The role and regulation of blebs in cell migration. *Current Opinion In Cell Biology*, 25(5):582–590, oct 2013.
- [48] M. J. Paszek, C. C. DuFort, O. Rossier, R. Bainer, J. K. Mouw, K. Godula, J. E. Hudak, J. N. Lakins, A. C. Wijekoon, L. Cassereau, M. G. Rubashkin, M. J. Magbanua, K. S. Thorn, M. W. Davidson, H. S. Rugo, J. W. Park, D. A. Hammer, G. Giannone, C. R. Bertozzi, and V. M. Weaver. The cancer glycocalyx mechanically primes integrin-mediated growth and survival. *Nature*, 511(7509):319–325, apr 2015.
- [49] B. Peleg, A. Disanza, G. Scita, and N. Gov. Propagating Cell-Membrane Waves Driven by Curved Activators of Actin Polymerization. *PLoS ONE*, 6(4):e18635, apr 2011.
- [50] B. Peng, V. Gaspar, and K. Showalter. False Bifurcations in Chemical Systems: Canards. *Philosophical Transactions of the Royal Society A: Mathematical, Physical and Engineering Sciences*, 337(1646):275–289, 1991.
- [51] J. Peukes and T. Betz. Direct Measurement of the Cortical Tension during the Growth of Membrane Blebs. *Biophysj*, 107(8):1810–1820, oct 2014.
- [52] S. Qi, M. Krogsgaard, M. M. Davis, and A. K. Chakraborty. Molecular flexibility can influence the stimulatory ability of receptor-ligand interactions at cell-cell junctions. *Proceedings Of The National Academy Of Sciences Of The United States Of America*, 103(12):4416–4421, mar 2006.

- [53] P. Rangamani, A. Benjamini, A. Agrawal, B. Smit, D. J. Steigmann, and G. Oster. Small scale membrane mechanics. *Biomechanics and Modeling in Mechanobiology*, oct 2013.
- [54] G. L. Ryan, H. M. Petroccia, N. Watanabe, and D. Vavylonis. Excitable Actin Dynamics in Lamellipodial Protrusion and Retraction. *Biophysical Journal*, 102(7):1493–1502, apr 2012.
- [55] G. L. Ryan, N. WATANABE, and D. Vavylonis. A review of models of fluctuating protrusion and retraction patterns at the leading edge of motile cells. *Cytoskeleton (Hoboken, N.J.)*, 69(4):195–206, feb 2012.
- [56] G. Salbreux, J. Prost, and J. F. Joanny. Hydrodynamics of Cellular Cortical Flows and the Formation of Contractile Rings. *Physical Review Letters*, 103(5):58102, jul 2009.
- [57] J. Sedzinski, M. Biro, A. Oswald, J.-Y. Tinevez, G. Salbreux, and E. Paluch. Polar actomyosin contractility destabilizes the position of the cytokinetic furrow. *Nature*, 476(7361):462–466, aug 2011.
- [58] W. Strychalski, C. A. Copos, O. L. Lewis, and R. D. Guy. A poroelastic immersed boundary method with applications to cell biology. *Journal of Computational Physics*, 282(C):77–97, feb 2015.
- [59] W. Strychalski and R. D. Guy. A computational model of bleb formation. *Mathematical Medicine and Biology*, 30(2):115–130, jun 2013.
- [60] W. Strychalski and R. D. Guy. Intracellular Pressure Dynamics in Blebbing Cells . 2015.
- [61] J. N. Thon, H. Macleod, A. J. Begonja, J. Zhu, K.-C. Lee, A. Mogilner, J. H. Hartwig, and J. E. Italiano. Microtubule and cortical forces determine platelet size during vascular platelet production. *Nature Communications*, 3:852–859, may 2012.
- [62] J.-Y. Tinevez, U. Schulze, G. Salbreux, J. Roensch, J.-F. Joanny, and E. Paluch. Role of cortical tension in bleb growth. *Proceedings Of The National Academy Of Sciences Of The United States Of America*, 106(44):18581–18586, nov 2009.
- [63] R. Wollman and T. Meyer. Coordinated oscillations in cortical actin and Ca²⁺ correlate with cycles of vesicle secretion. *Nature Cell Biology*, 14(12):1261–1269, nov 2012.
- [64] T. E. Woolley, E. A. Gaffney, and A. Goriely. Membrane shrinkage and cortex remodelling are predicted to work in harmony to retract blebs. *Royal Society Open Science*, 2(7):150115–150184, jul 2015.
- [65] T. E. Woolley, E. A. Gaffney, J. M. Oliver, R. E. Baker, S. L. Waters, and A. Goriely. Cellular blebs: pressure-driven, axisymmetric, membrane protrusions. *Biomechanics and Modeling in Mechanobiology*, 13(2):463–476, jul 2013.

- [66] T. E. Woolley, E. A. Gaffney, S. L. Waters, J. M. Oliver, R. E. Baker, and A. Goriely. Three mechanical models for blebbing and multi-blebbing. *IMA Journal of Applied Mathematics*, 79(4):636–660, jul 2014.
- [67] Y. Xiong, C.-H. Huang, P. A. Iglesias, and P. N. Devreotes. Cells navigate with a local-excitation, global-inhibition-biased excitable network. *Proceedings Of The National Academy Of Sciences Of The United States Of America*, 107(40):17079–17086, oct 2010.
- [68] J. Young and S. Mitran. A numerical model of cellular blebbing: A volume-conserving, fluid{–}structure interaction model of the entire cell. *Journal of Biomechanics*, 43(2):210–220, jan 2010.
- [69] C. Zhu. Mechanochemistry: A Molecular Biomechanics View of Mechanosensing. *Annals of Biomedical Engineering*, 42(2):388–404, sep 2013.

A. Appendices

A.1 Cell surface mechanochemistry and the determinants of bleb formation, healing and travel velocity

A.1.1 Summary of experimental predictions

The model makes several testable predictions. For convenience, we tabulate these predictions here. Note that these predictions presume that the cell is exhibiting blebs before the perturbation.

Table A.1: Model predictions for experimental perturbations.

Experimental perturbation	Parameter	Prediction
Increasing hydrostatic pressure	$P \uparrow$	Larger blebs
Increasing molecular size of adhesion molecules	$D \uparrow$	Abolish blebbing
Decreasing molecular size of adhesion molecules	$D \downarrow$	Slower bleb healing
Increasing myosin contractility	$M \uparrow$	Abolish blebbing
Decreasing myosin contractility	$M \downarrow$	Slower bleb healing
Increasing membrane tension	$\gamma_M \uparrow$	Faster bleb travel
Increasing abundance of adhesions	$k_{on} \uparrow$	Slower bleb travel

A.1.2 Details of geometry of cortical and cytoplasmic actin

In 3D, the cell surface and cortex are curved, discontinuous two-dimensional manifolds and the cytoplasm is a 3D field. In full generality, the cortex and cytoplasmic actin network have a density at each point in space. We assume that actin-myosin contractility is isotropic and generates local stress proportional to the local density of cortical actin c . This stress therefore has two components: a tangential component due to connection with nearby cortex

$$\sigma_t = \sigma_m w_c c \nabla y_C, \quad (\text{A.1})$$

and a normal stress due to connection with the cytoplasmic actin network

$$\sigma_n = \sigma_m c y_C. \quad (\text{A.2})$$

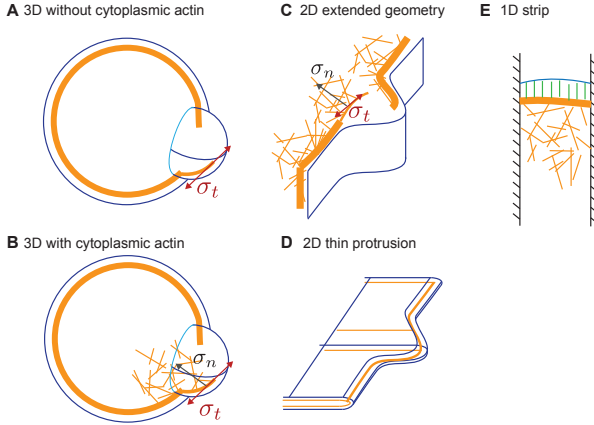


Figure A.1: Approximations of cortex and cytoplasmic actin geometry in 3D. (A-B) Bleb geometry in 3D including only tangential cortical contractility (A), and both tangential and normal contractility (B). (C-D) Representation of 2D model. (E) Hypothetical 1D “non-spatial” model corresponding to ODE system used in this project.

We find that the normal contractile force is necessary for asymmetric bleb healing, as occurs during bleb travel. This necessity can be understood from Fig. A.1: In the absence of cytoplasmic actin, the tangential stress pulls the membrane tangentially, but there is no force driving the cortex into the place of the cell.

Our goal is to understand in 3D. To this end, we find it informative to study simplified 2D systems and 1D systems as an analytical tool. The 2D model is equivalent to either the geometries shown in Fig. A.1C or D. The 1D model, which we refer to as the ODE model in the Main Text, corresponds to the geometry shown in Fig. A.1E.

A.1.3 Parameter estimation

Table A.2: Estimates of parameters used in non-dimensionalization.

Model parameter	Estimated value	Source
r	$0.1/\text{s}$	[25]
k_{on}	$100/\mu\text{m}^2 \cdot \text{s}$	[13]
k_{off}	$1/\text{s}$	[25]
κ	$10\text{ pN}/\mu\text{m}$	[13]
σ_m	$0.1\text{ Pa}/\mu\text{m}^2$	[13]
$\hat{\Pi}$	$100\text{ Pa}/\mu\text{m}$	[13]
y_M^0	$3\mu\text{m}$	[16]
γ_M	$100\text{ pN}/\mu\text{m}$	[51]

Using these estimates, the correspondence between dimensional and non-dimensional

parameters are given by

$$x = \chi \cdot 0.2 \mu\text{m} \quad (\text{A.3})$$

$$t = \tau \cdot 10s \quad (\text{A.4})$$

$$a = A \cdot 100/\mu\text{m}^2 \quad (\text{A.5})$$

$$y_M = Y_M \cdot 3 \mu\text{m} \quad (\text{A.6})$$

$$y_C = Y_C \cdot 3 \mu\text{m}. \quad (\text{A.7})$$

Note that model parameters not included in Table A.2 do not impact the non-dimensionalization.

To perform the parameter-space exploration in Fig. 5, we used ranges shown in Table A.3.

Table A.3: Dimensional parameters with ranges explored in simulation.

Parameter	Range explored for velocity plot
ω	0.0004 – 0.0006 [A.U.] · s ⁻¹
r	0.01 – 0.25 s ⁻¹
k_{on}	95 – 140 μm ⁻² s ⁻¹
k_{off}	0.5 – 1.05 s ⁻¹
δ	0.14 – 0.17 μm
κ	9 – 13 pN/ μm
f_0	5 – 20 pN
σ_m	550 – 725 Pa/ [A.U.]
$\hat{\Pi}$	65 – 105 Pa/ μm
γ_M	10 – 400 pN/ μm

A.1.4 Model variants

Bending

The inclusion of higher-order derivatives in the mechanical energy transform the system into a higher-order boundary value problem. For example, the bending energy term transforms the membrane shape equation to a fourth-order equation. We simulate the base model with the addition of bending terms $B > 0$, where the nondimensional bending modulus is $B \equiv \beta/\gamma x_c^3$. Results are shown in Fig. A.2. We find that the excitable parameter regime and traveling parameter regimes are unchanged. For $B = 100$, the velocity of travel is increased by approximately two-fold and healing is delayed compared to no bending.

Part-local, part-global pressure models

In the Main Text, we present models in which pressure is either purely global (one quantity is shared among the entire domain) or purely local (a local increase in y_M leads to a local drop in pressure, and no where else). However, recent evidence from computational models [60] suggests that in a poroelastic cytoplasm, local membrane extension may lead to a large local

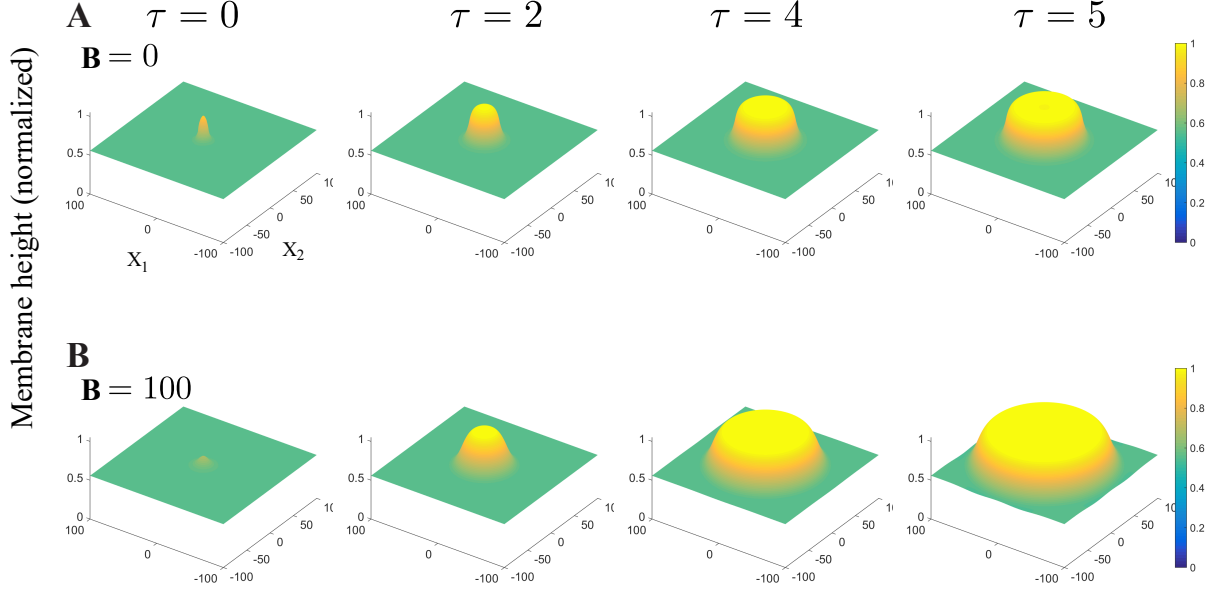


Figure A.2: Influence of membrane bending rigidity. (A) Traveling bleb on a uniform surface with no bending energy $B = 0$. (B) Traveling bleb with large bending rigidity $B = 100$. The bleb velocity is increased by approximately two-fold and healing is delayed (but eventually occurs, not shown).

pressure drop and a smaller global pressure drop. To address this possibility, we simulate model variants in which the pressure drop is part local and part global.

- Local-global additive:

$$\Pi(x_1, x_2) = \hat{\Pi} \left(\left(1 - \frac{y_M(x_1, x_2)}{y_M^0} \right) + \epsilon_p \iint \left(1 - \frac{y_M(\tilde{x}_1, \tilde{x}_2)}{y_M^0} \right) d\tilde{x}_1 d\tilde{x}_2 \right) \quad (\text{A.8})$$

- Local-global multiplicative pressure:

$$\Pi(x_1, x_2) = \hat{\Pi} \cdot \left(1 - \frac{y_M(x_1, x_2)}{y_M^0} \right) \cdot \iint \left(1 - \frac{y_M(\tilde{x}_1, \tilde{x}_2)}{y_M^0} \right) d\tilde{x}_1 d\tilde{x}_2 \quad (\text{A.9})$$

Results are shown in Fig. ???. As expected, when the global component of pressure drop is small, simulation results are similar to purely-local pressure, with blebs expanding outward as an expanding annulus. As intermediate global components, the global pressure drop is enough to collapse the bleb as its area increases. No symmetry breaking is observed.

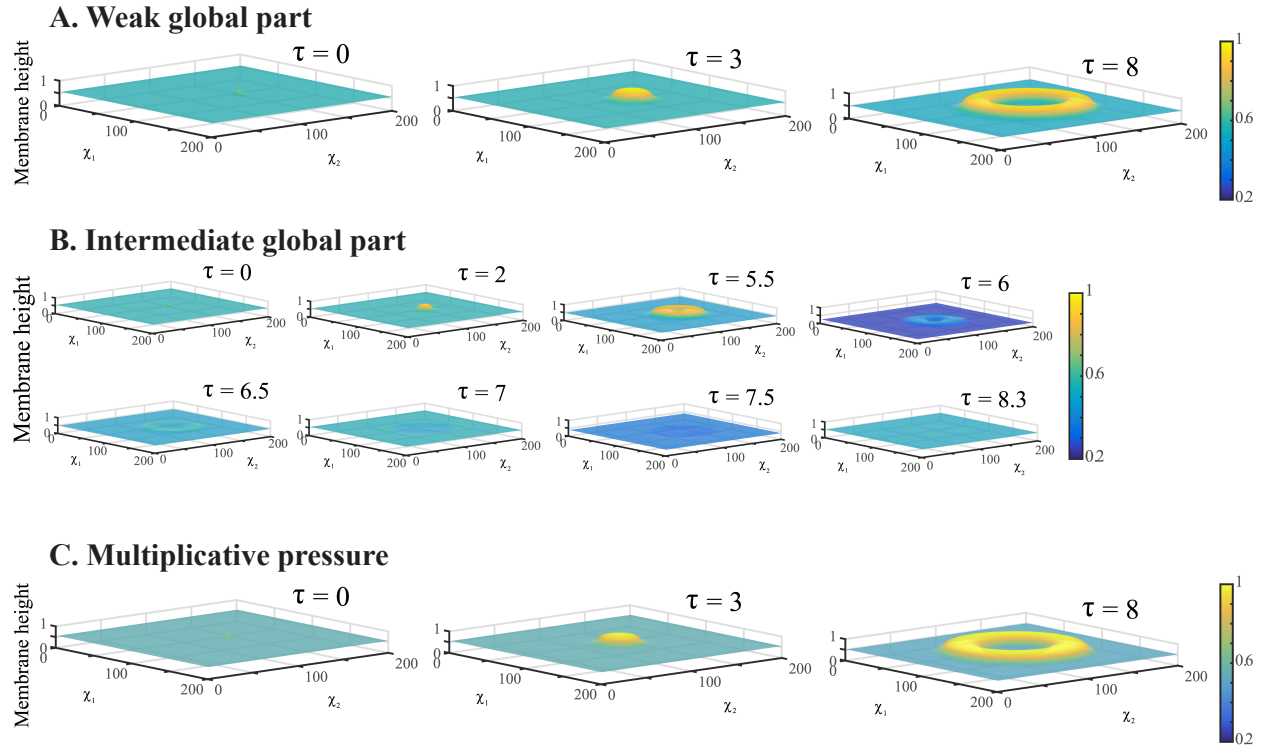


Figure A.3: Simulations assuming that local membrane protrusion leads to both local and global pressure drops. (A) Additive pressure Eq. A.8 with weak global part, $\epsilon_p = 0.1$. (B) Additive pressure with intermediate global part, $\epsilon_p = 0.18$. (C) Multiplicative pressure.

A.1.5 Details of numerical method

A.1.6 Base model

The base model, Eqs. 10-13, comprise a two-dimensional boundary value problem of elliptic type at each instant in time, coupled to two first-order (in time) partial differential equations. To solve the base model, we discretize space into a uniform grid of width $\Delta\chi = 0.1$ and time step size $\Delta\tau = 0.01$. We use a standard five-point stencil finite difference method in space and forward-Euler in time.

A.1.7 Non-uniform tension

The inclusion of non-uniform tension changes the boundary value problem to a non-uniform elliptic equation. The equations takes the form

$$P = f(\chi_1, \chi_2)Y_M(\chi_1, \chi_2) - \nabla \cdot (\Gamma(\chi_1, \chi_2)\nabla Y_M(\chi_1, \chi_2)) \quad (\text{A.10})$$

where f and Γ are spatially varying. We use a uniform grid in space and set $\Delta\chi = 0.1$. The functions f, Y_M and Γ all live at cell edges ($f|_{i,j} = f(i\Delta\chi, j\Delta\chi)$, $i = 1, 2, \dots, 2000$)

and we impose periodic boundary conditions. The parameter functions f and Γ must be interpolated to the edges, which we do by uniform averaging. The resulting discretization stencil is given by

$$\begin{aligned} P = & \left(f|_{i,j} + \frac{1}{2\Delta x^2} (\Gamma|_{i+1,j} + \Gamma|_{i-1,j} + \Gamma|_{i,j+1} + \Gamma|_{i,j-1} + 4\Gamma|_{i,j}) \right) \mathbf{Y}_M|_{i,j} \\ & - \frac{1}{2\Delta x^2} ((\Gamma|_{i+1,j} + \Gamma|_{i,j}) \mathbf{Y}_M|_{i+1,j} + (\Gamma|_{i,j} + \Gamma|_{i,j-1}) \mathbf{Y}_M|_{i-1,j}) \\ & - \frac{1}{2\Delta x^2} ((\Gamma|_{i,j} + \Gamma|_{i,j+1}) \mathbf{Y}_M|_{i,j+1} + (\Gamma|_{i,j} + \Gamma|_{i,j-1}) \mathbf{Y}_M|_{i,j-1}) \end{aligned}$$

Since this equation remains linear, it can be written into a sparse matrix and solved as a linear system.

A.1.8 Higher-order models including bending forces

Adding higher order terms, including bending forces, transforms the boundary value problem into a higher-order boundary value problem. The bending term, in particular, introduces a fourth-order bilaplacian operator. This significantly increases the computational cost of solving the equations, therefore we use a more sophisticated solver described here. We solve the following equations:

$$\frac{\partial C}{\partial \tau} = \Omega A - C \quad (\text{A.11})$$

$$\epsilon \frac{\partial A}{\partial \tau} = \frac{C}{1+C} \exp \left(- \left(\frac{1}{D} \frac{MC}{A+MC} Y_M \right) \right) - A \exp \left(\frac{1}{F_0} \frac{MC}{A+MC} Y_M \right) \quad (\text{A.12})$$

$$P = h Y_m - \nabla \cdot (\Gamma \nabla Y_M) + B \nabla^4 Y_M \quad (\text{A.13})$$

$$h = \frac{AMC}{A+MC} + P, \quad (\text{A.14})$$

where $\Omega = 57$, $\epsilon = 0.1$, $D = 0.15$, $F_0 = 1$, $M = 0.007$ and $P = 0.1$. In non-uniform tension models, $B = 0$ and the non-uniform tension term $\Gamma = 1 + \theta C$ where $\theta = 0.1$ or $\theta = 0.2$. For bending models, $\Gamma = 1$ and $B \in \{10^{-2}, 10^{-1}, 1, 10^1, 10^2\}$.

All variables satisfy periodic conditions at all boundaries. The initial condition for Y_M and C is their steady state value $Y_M^{ss} = 0.5582$ and $C^{ss} = 15.8236$. A is also set to steady state $A^{ss} = 0.2776$ except where the bleb is triggered on a $5\chi \times 5\chi$ patch where $A = 0$.

The system is solved in a square computational domain $[-200, 200]^2$. The domain is initialized to a 64×64 mesh with a maximum of 5 refinement levels. At the finest level, grid length is $400/(64 \times 2^5) \approx 0.2$. The time step is 10^{-2} .

We use the implicit second order Crank-Nicholson scheme for time discretization in eqs. (A.11) and (A.12). Spatial derivatives are discretized using central difference approximations. eq. (A.13) is reformulated as a system of two second order equations. Block structured Cartesian refinement is used to efficiently resolve the multiple spatial scales. In particular, the mesh is refined in regions with large spatial gradients of Y_M (typically around the bleb). The equations at implicit time level are solved by the adaptive nonlinear multigrid method

developed in [?].

A.2 Nuclear blebs

A.2.1 Non-dimensionalization

Characteristic scales

$$\begin{aligned} a^c &= b_{tot}/\mathcal{L}_0 \\ b^c &= b_{tot}/\mathcal{L}_0 \\ a_{nuc}^c &= \frac{k_{off}^{0b}}{k_{on}^b} \frac{b_{tot}}{\mathcal{L}_0} \frac{\mathcal{L}_0^2}{4\pi} \\ b_{nuc}^c &= \frac{k_{off}^{0b}}{k_{on}^b} \frac{b_{tot}}{\mathcal{L}_0} \frac{\mathcal{L}_0^2}{4\pi} \\ t^c &= 1/k_{off}^{0b} \\ s^c &= \mathcal{L}_0/(2\sqrt{\pi}) \\ \mathcal{E}^c &= \mathcal{G}_b(b^c)\mathcal{L}_0/(2\sqrt{\pi}) \end{aligned}$$

Let

$$\begin{aligned} A &= a/a^c \\ B &= b/b^c \\ A_{nuc} &= a_{nuc}/a_{nuc}^c \\ B_{nuc} &= b_{nuc}/b_{nuc}^c \\ \tau &= t/t^c \\ S &= s/s^c \\ \vec{\chi} &= \vec{x}/s^c \\ E &= \mathcal{E}/\mathcal{E}^c \end{aligned}$$

Then

$$\begin{aligned} \frac{\partial A}{\partial \tau} &= \frac{\mathcal{L}_0}{b_{tot}k_{off}^{0b}} \left(\frac{k_{on}^a}{\mathcal{A}(t)} A_{nuc} \frac{k_{off}^{0b}}{k_{on}^b} \frac{b_{tot}}{\mathcal{L}_0} \frac{\mathcal{L}_0^2}{4\pi} - k_{off}^a(s, b) A \frac{b_{tot}}{\mathcal{L}_0} \right) = \frac{k_{on}^a}{k_{on}^b} \frac{\mathcal{L}_0^2}{4\pi \mathcal{A}(t)} A_{nuc} - \frac{k_{off}^a(s, b)}{k_{off}^{0b}} A \\ \frac{\partial B}{\partial \tau} &= \frac{\mathcal{L}_0}{b_{tot}k_{off}^{0b}} \left(\frac{k_{on}^b}{\mathcal{A}(t)} B_{nuc} \frac{k_{off}^{0b}}{k_{on}^b} \frac{b_{tot}}{\mathcal{L}_0} \frac{\mathcal{L}_0^2}{4\pi} - k_{off}^b(s, a) B \frac{b_{tot}}{\mathcal{L}_0} \right) = \frac{\mathcal{L}_0^2}{4\pi \mathcal{A}(t)} B_{nuc} - \frac{k_{off}^b(s, b)}{k_{off}^{0b}} B \\ \rightarrow \text{ let } \kappa_{on} &= \frac{k_{on}^a}{k_{on}^b}, \lambda(\tau) = \frac{4\pi \mathcal{A}(t)}{\mathcal{L}_0^2}, \phi_A(S, B) = \frac{\Phi_a(S, B)}{k_{off}^{0b}}, \phi_B(S, A) = \frac{\Phi_b(S, A)}{k_{off}^{0b}}, \kappa_{off} = \frac{k_{off}^{0a}}{k_{off}^{0b}} \\ \Rightarrow \frac{\partial A}{\partial \tau} &= \kappa_{on} \frac{1}{\lambda(\tau)} A_{nuc} - (\kappa_{off} + \phi_A(S, B)) A, \\ \frac{\partial B}{\partial \tau} &= \frac{1}{\lambda(\tau)} B_{nuc} - (1 + \phi_B(S, A)) B \end{aligned}$$

And

$$\begin{aligned}
E &= \frac{\mathcal{E}_{stretch} + \mathcal{E}_{pressure} + \mathcal{E}_{bending} + \mathcal{E}_{cytoskeleton} + k_B T \xi}{\mathcal{G}_b(b^c) \mathcal{L}_0 / (2\sqrt{\pi})} \\
E_{stretch} &= \frac{\int_0^{\mathcal{L}_0} \frac{1}{2} (\mathcal{G}_a(a(s)) + \mathcal{G}_b(b(s))) \left(\left\| \frac{\partial \vec{x}}{\partial s} \right\| - 1 \right)^2 ds}{\mathcal{G}_b(b^c) \mathcal{L}_0 / (2\sqrt{\pi})} \\
&= \frac{\int_0^{2\sqrt{\pi}} \frac{1}{2} (\mathcal{G}_a(A(S)a^c) + \mathcal{G}_b(B(S)b^c)) \left(\left\| \frac{\partial \vec{\chi}}{\partial S} \right\| - 1 \right)^2 \frac{\mathcal{L}_0}{2\sqrt{\pi}} dS}{\mathcal{G}_b(b^c) \mathcal{L}_0 / (2\sqrt{\pi})} \\
&\text{let } G_A(A(S)) = \frac{\mathcal{G}_a(A(S)a^c)}{\mathcal{G}_b(b^c)}, G_B(B(S)) = \frac{\mathcal{G}_b(B(S)b^c)}{\mathcal{G}_b(b^c)} \\
\Rightarrow E_{stretch} &= \int_0^{2\sqrt{\pi}} \frac{1}{2} (G_A(A(S)) + G_B(B(S))) \left(\left\| \frac{\partial \vec{\chi}}{\partial S} \right\| - 1 \right)^2 dS \\
E_{pressure} &= \frac{\mathcal{P} \left(\frac{\lambda(\tau)}{\lambda_0} - 1 \right)^2}{\mathcal{G}_b(b^c) \mathcal{L}_0 / (2\sqrt{\pi})} = \Pi \left(\frac{\lambda(\tau)}{\lambda_0} - 1 \right)^2 \\
&\text{where } \lambda_0 = \frac{4\pi \mathcal{A}_0}{\mathcal{L}_0^2}, \text{ and let } \Pi = \frac{\mathcal{P}}{\mathcal{G}_b(b^c) \mathcal{L}_0 / (2\sqrt{\pi})} \\
E_{bending} &= \frac{\int_0^{\mathcal{L}_0} \frac{1}{2} (\mathcal{M}_a(a(s)) + \mathcal{M}_b(b(s))) \left\| \frac{\partial^2 \vec{x}}{\partial s^2} \right\|^2 ds}{\mathcal{G}_b(b^c) \mathcal{L}_0 / (2\sqrt{\pi})} \\
&= \frac{\int_0^{2\sqrt{\pi}} \frac{1}{2} (\mathcal{M}_a(A(S)a^c) + \mathcal{M}_b(B(S)b^c)) \left\| \frac{2\sqrt{\pi}}{\mathcal{L}_0} \frac{\partial^2 \vec{\chi}}{\partial S^2} \right\|^2 \frac{\mathcal{L}_0}{2\sqrt{\pi}} dS}{\mathcal{G}_b(b^c) \mathcal{L}_0 / (2\sqrt{\pi})} \\
&\text{let } M_A(A(S)) = \frac{4\pi \mathcal{M}_a(A(S)a^c)}{\mathcal{G}_b(b^c) \mathcal{L}_0^2}, M_B(B(S)) = \frac{4\pi \mathcal{M}_b(B(S)b^c)}{\mathcal{G}_b(b^c) \mathcal{L}_0^2} \\
\Rightarrow E_{bending} &= \int_0^{2\sqrt{\pi}} \frac{1}{2} (M_A(A(S)) + M_B(B(S))) \left\| \frac{\partial^2 \vec{\chi}}{\partial S^2} \right\|^2 dS \\
E_{cytoskeleton} &= \frac{\int_0^{\mathcal{L}_0} \mathcal{F}_{cyto}(a(s)) \Theta(\theta) \| \vec{x} \| ds}{\mathcal{G}_b(b^c) \mathcal{L}_0 / (2\sqrt{\pi})} \\
&= \frac{\int_0^{2\sqrt{\pi}} \mathcal{F}_{cyto}(A(S)a^c) \Theta(\theta) \left\| \frac{\mathcal{L}_0}{2\sqrt{\pi}} \vec{\chi} \right\| \frac{\mathcal{L}_0}{2\sqrt{\pi}} dS}{\mathcal{G}_b(b^c) \mathcal{L}_0 / (2\sqrt{\pi})} \\
&\text{let } F_{cyto}(A(S)) = \frac{\mathcal{F}_{cyto}(A(S)a^c) \mathcal{L}_0}{2\sqrt{\pi} \mathcal{G}_b(b^c)} \\
\Rightarrow E_{cytoskeleton} &= \int_0^{2\sqrt{\pi}} F_{cyto}(A(S)) \Theta(\theta) \| \vec{\chi} \| dS \\
&\text{let } k_B T = \frac{k_B \mathcal{T}}{\mathcal{G}_b(b^c) \mathcal{L}_0 / (2\sqrt{\pi})} \\
\Rightarrow E &= E_{stretch} + E_{pressure} + E_{bending} + E_{cytoskeleton} + k_B T \xi
\end{aligned}$$